PASJ: Publ. Astron. Soc. Japan , 1–**??**,

SiO Maser Survey off the Galactic Plane: A Signature of Streaming Motion

Shuji Deguchi[1,2], Tomomi Shimoikura[1,3],
and
Kazutaka Koike[1,2]
[1] *Nobeyama Radio Observatory, National Astronomical Observatory, Minamimaki, Minamisaku, Nagano 384-1305*
[2] *Graduate University for Advanced Studies, National Astronomical Observatory, Minamimaki, Minamisaku, Nagano 384-1305*
[3] *current address: Department of Astronomy and Earth Sciences, Tokyo Gakugei University, Koganei, Tokyo 184-8501*

(PASJ 62 No.3, 2010 June 25 isuue in press)

(Received 2009 September 28; accepted 2009 February 27)

Abstract

A group of Mira variables in the solar neighborhood show unusual spatial motion in the Galaxy. To study this motion in much larger scale in the Galaxy, we newly surveyed 134 evolved stars off the Galactic plane by SiO maser lines, obtaining accurate radial velocities of 84 detected stars. Together with the past data of SiO maser sources, we analyzed the radial velocity data of a large sample of sources distributing in a distance range of about 0.3 – 6 kpc in the first Galactic quadrant. At the Galactic longitudes between 20 and 40°, we found a group of stars with large negative radial velocities, which deviate by more than 100 km s^{-1} from the Galactic rotation. We show that these deviant motions of maser stars are created by periodic gravitational perturbation of the Bulge bar, and that the effect appears most strongly at radii between corotation and outer Lindblad resonances. The resonance effect can explain the displacement of positions from the Galactic plane as well.

Key words: Galaxy: disk, Galaxy: kinematics and dynamics, stars: AGB and post-AGB

1. Introduction

Stellar OH and SiO maser sources are powerful probes of Galactic structure and stellar evolution (Habing et al 2006; Deguchi 2008). Radial velocity databases of these sources are useful to investigate dynamical motions of stars in the Galactic disk and Bulge (Izumiura et al. 1995; Sevenster et al. 2001; Deguchi et al. 2004; Fujii et al. 2006). Because of a recent progress of studies of tidal streams surrounding our Galaxy and in the solar neighborhood (Belokurov et al. 2007; Grillmair 2009), one of urgent issues in this field is to separate a Bulge-bar resonance stream from tidal streams of relic dwarf galaxies in the radial velocity data.

It has been known that the Galactic disk has two components, thick and thin; the former has a thickness of 1 – 2 kpc involving metal-poor stars and kinematically peculiar stars, while the latter has a thickness of about 300 pc involving young new populations. A hypothesis that the thick disk is a relic of past merging processes has been proposed for the origin of thick disk (Helmi et al. 1999; Navarro et al. 2004; Helmi et al. 2006).

Moving groups in the solar neighborhood have also been known, and they are considered to be fossils keeping dynamical information of their birth. Two famous examples are the Arcturus and Hercules groups of stars (Eggen 1996); the former is a group of metal poor stars with a coherent spatial motion with a ~ 100 km s^{-1} lag to the Galactic rotation, and the latter is a stellar group with a heterogeneous mixture of metal abundances and with a smaller rotational lag. Spatial motions of these moving groups are well investigated optically based on the Hipparcos (proper motions) and the RAVE (the radial velocities) databases. However, these investigations have a limitation of distance up to about 1 kpc due to lack of proper motion data. Because of heterogenous metal abundances of member stars, the origin of the Hercules stream is attributed to a resonance of the bar-like Bulge (Bensby et al. 2007). Feast & Whitelock (2000) investigated an outward motion of short-period Mira variables near the Sun, and attributed it to the resonance effect of the Bulge bar.

In this paper, we reinvestigate the radial velocity data of SiO maser sources toward the region of $l = 20 - 60°$, and $-30 < b < 60°$ (excluding the galactic plane, $|b| < 3°$). In this region, Deguchi et al. (2007) found a group of SiO maser stars with large negative velocities ($v_{\rm LSR} \sim -70$ km s^{-1}), which may be attributed to a resonance effect of the Bulge bar or a relic streaming motion. However, the previous off-plane SiO search was aimed to find distant debris stars such as those in the Sgr dwarf streams, the search was somewhat shallow in depth except toward Sgr dwarf

streams. Therefore, we have made a new sensitive observation by SiO maser lines toward the thick disk, and have added more data in radial velocity database. Here, we analyze kinematics of this SiO maser star stream, and test if this stream is originated by the gravitational perturbation of the Bulge bar.

2. Observational results

The observations were made with the 45m radio telescope at Nobeyama in 2009 April and May by the SiO $J=1$–0 $v=1$ and 2 transitions at 43.122 and 42.821 GHz, respectively. Cooled HEMT receiver (H40) was used for the 43 GHz observations with acousto-opt spectrometer arrays with the 40 and 250 MHz bandwidths (velocity resolution of about 0.3 and 1.8 km s^{-1}, respectively). The overall system temperature was about 180 — 250 K for the SiO observations depending on weather conditions. The half-power beam width (HPBW) of the telescope was about 40″ at 43 GHz. The conversion factor of the antenna temperature to the flux density was about 2.9 Jy K^{-1}. All of the observations were made by the position-switching mode. Further details of observations using the NRO 45-m telescope have been described elsewhere (Deguchi et al. 2000).

The sample for SiO searches was chosen in the area within $20^\circ < l < 60^\circ$ and $|b| < 45^\circ$ (excluding $|b| < 3^\circ$) by the selection criteria which have been established well in the past SiO surveys. The mid-infrared objects brighter than 3 Jy at 12 μm, and the color $-0.5 < C_{12}[\equiv log(F_{25}/F_{12})] \lesssim 0.2$ were selected from IRAS point source catalog (Joint IRAS Science Working Group 1988), where F_{12} and F_{25} are the IRAS flux densities in the 12 and 25 μm bands, respectively. The MSX bands C and E (Egan et al. 2003) were also consulted for the $|b| \lesssim 6^\circ$ sources. Then, we checked whether or not the MIR objects have a NIR counterpart in the 2MASS catalog (Cutri et al. 2003) with a customary selection criteria in our SiO maser searches (Deguchi et al. 2004): $K < 9$, and $H-K > 0.9$ for an initial sample. All the objects in the present sample have 2MASS counterpart brighter than $K = 8.2$ mag. These sources are supposedly late-type (AGB or post-AGB) stars with circumstellar dust in a color-temperature range between 250 and 1000 K. Excluding previously observed objects, we finally selected about 150 candidates which satisfied above criteria in this sky area. However, because of time restriction of observations, we completed half of these sources, for which we consumed all of the objects above $F_{12} = 5$ Jy. Furthermore, we added bright objects for backup (for bad weather condition), which involves slightly bluer sources in $H-K$ but not surveyed before. We added these additional objects to our results for completeness.

Observational results are summarized in tables 1 and 2 for SiO detection and no detection, respectively. The observed spectra of the SiO $J=1$–0 $v=1$ and 2 transitions are shown in figure 1a – 1e for the detections. Table 3 summarizes infrared properties of the observed sources. For a distance measure, we use the corrected K magnitude for interstellar and circumstellar reddening,

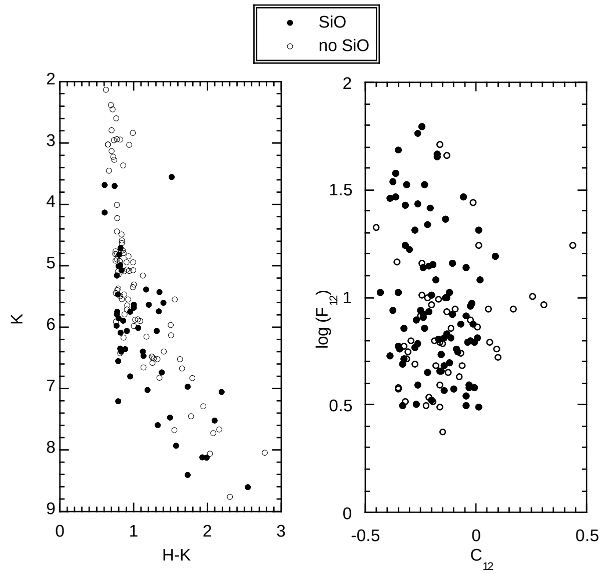

Fig. 2. NIR and MIR color-magnitude diagrams.

$$K_c = K - A_K/E(H-K) \times [(H-K) - (H-K)_0], \quad (1)$$

where we use $A_K/E(H-K) = 1.44$ and $(H-K)_0 = 0.5$, which is appropriate for M5III stars (Fujii et al. 2006). The corrected K_c is listed at the 6th column in table 3. A typical Mira star with a period of about 450 d located at the Galactic center (distance of 8 kpc) without extinction has $K_c = 6.43$ (Glass et al. 1995). We will use this value to estimate distances in the next section. Because SiO maser stars are mostly miras, the period–K_c relation [at 8 kpc; Glass et al. (1995)] gives a relatively smaller dispersion of about 1 magnitude in average K_c for the Bulge SiO maser stars [with an average period of $\sim$ 490d $\pm$ 130d ; see figure 3 of Deguchi et al. (2004)]. Because the single-epoch 2MASS photometric magnitude may differ from the average value by about 1 magnitude [e.g., Figure 11 of Messineo eta l. (2004)], and furthermore absolute K magnitude depends on the spectral type of a star (Wainscoat et al. 1992), we deduce that the error in distance in the present paper is a factor of more than 2.

Figure 2 shows the $K-H-K$ and $\log(F_{12}) - C_{12}$ diagrams for the observed sources. These panels show that the color-selection criteria described above can extract the SiO emitting objects quite effectively from the infrared star catalogs. Figure 3 shows histograms of $\log(F_{12})$ and K_c for the SiO detection and no detection. The SiO detection rate are quite high ($\sim$80 %) for bright infrared objects in F_{12} and K_c terms, but it decreases with decreasing infrared fluxes. Beyond $K_c > 5.5$, no detection surpasses the detection because of the large distance. These diagrams show properties similar to those made in the previous surveys in the Galactic plane (for example, Deguchi et al. 2004), and assure that the present survey off the Galactic plane was made appropriately.

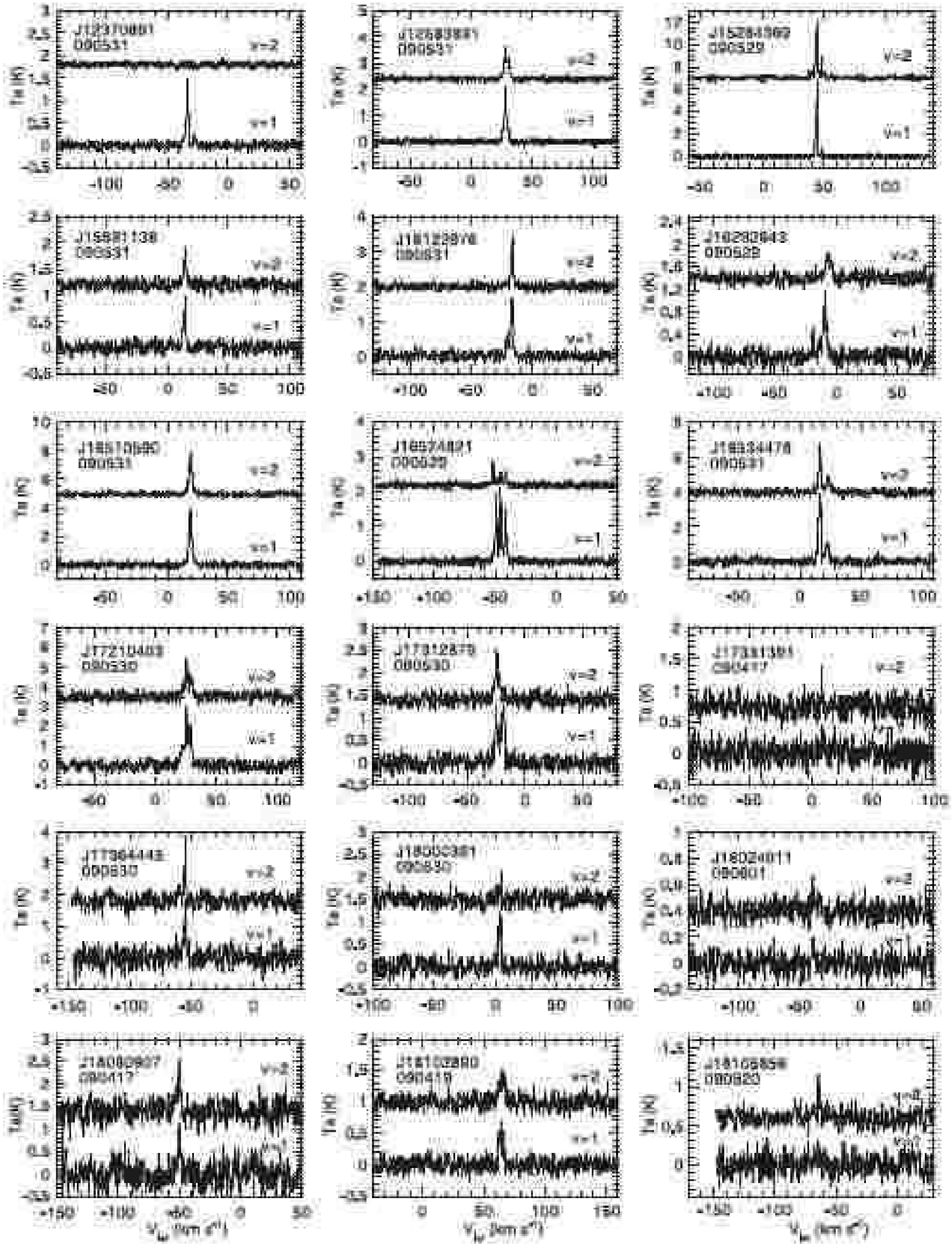

Fig. 1. a. SiO $J = 1$–0 $v = 1$ and 2 spectra. The source name (Jhhmmssss format) and the observed date (yymmdd format) are shown at the upper left of each panel.

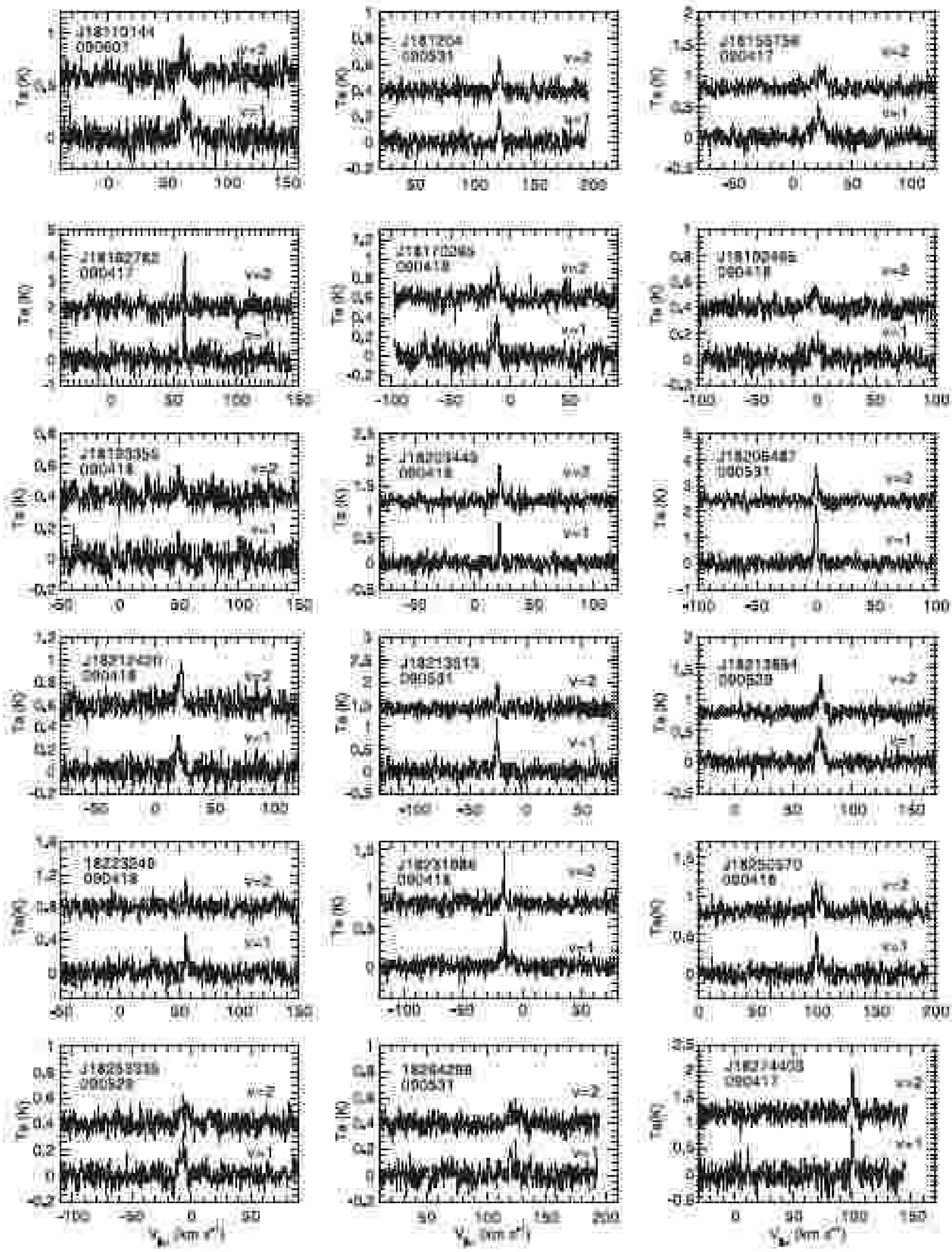

Fig. 1. b. SiO $J = 1$–0 $v = 1$ and 2 spectra. The source name (Jhhmmssss format) and the observed date (yymmdd format) are shown at the upper left of each panel.

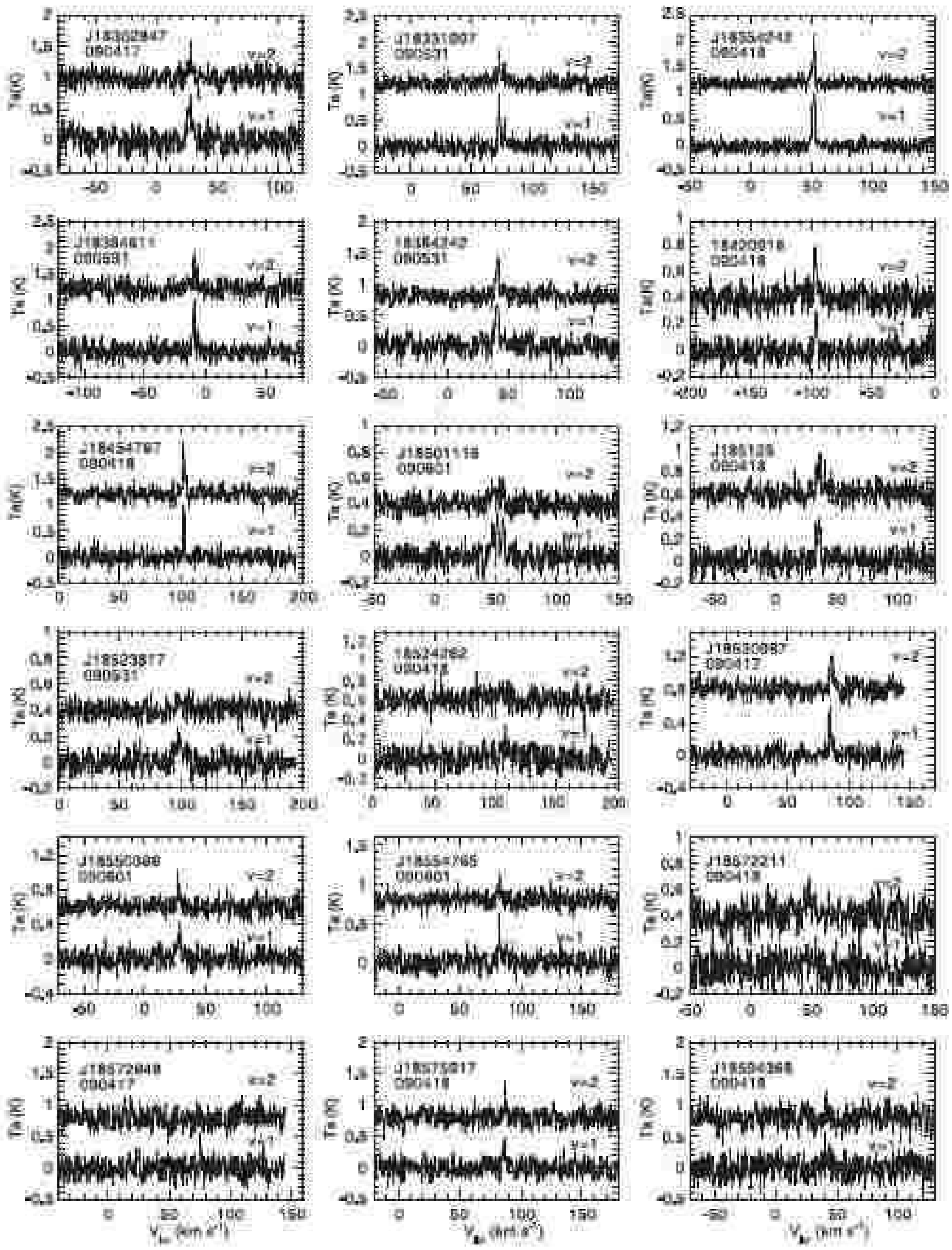

Fig. 1. c. SiO $J = 1$–0 $v = 1$ and 2 spectra. The source name (Jhhmmssss format) and the observed date (yymmdd format) are shown at the upper left of each panel.

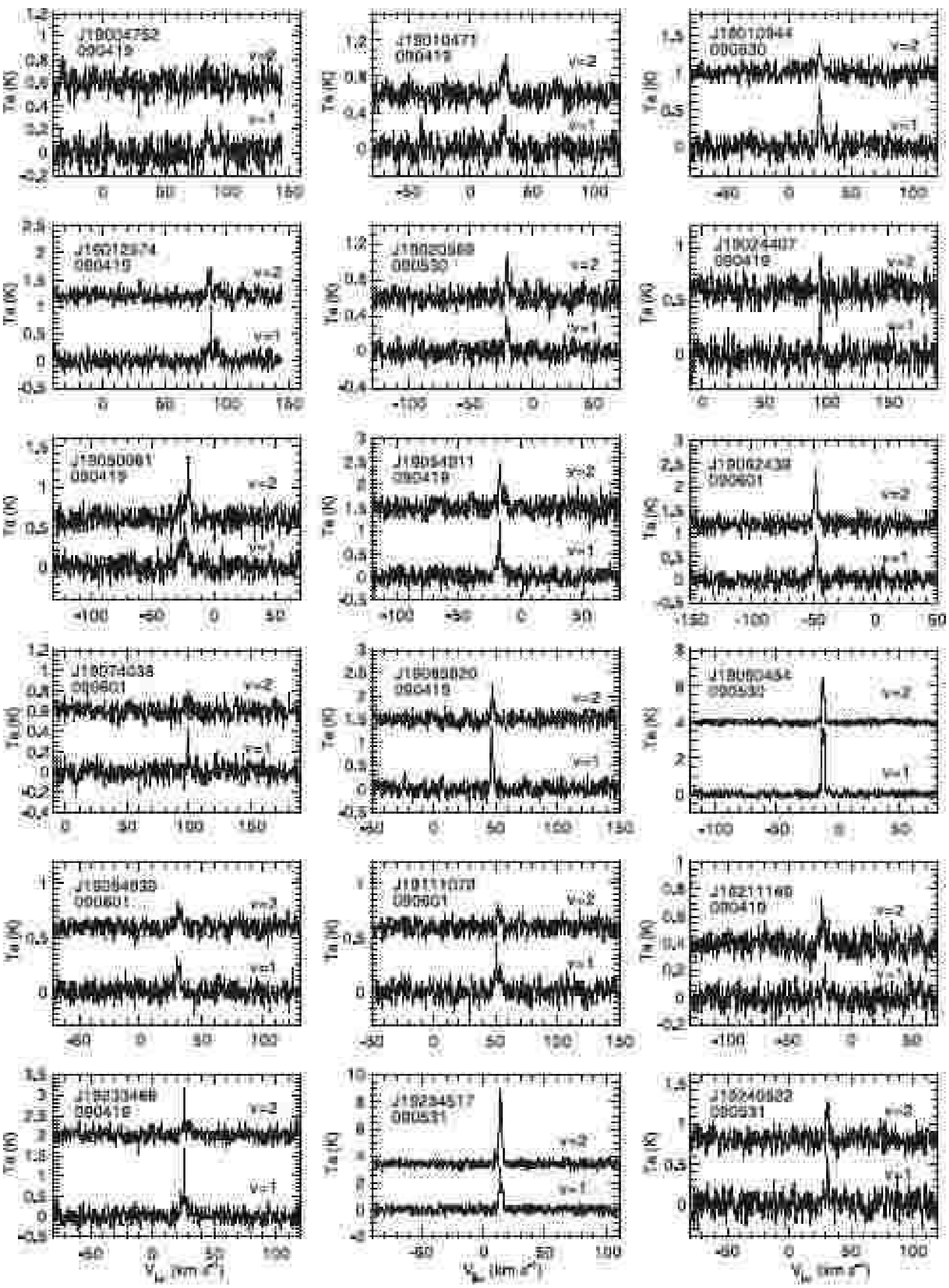

Fig. 1. d. SiO $J = 1$–0 $v = 1$ and 2 spectra. The source name (Jhhmmssss format) and the observed date (yymmdd format) are shown at the upper left of each panel.

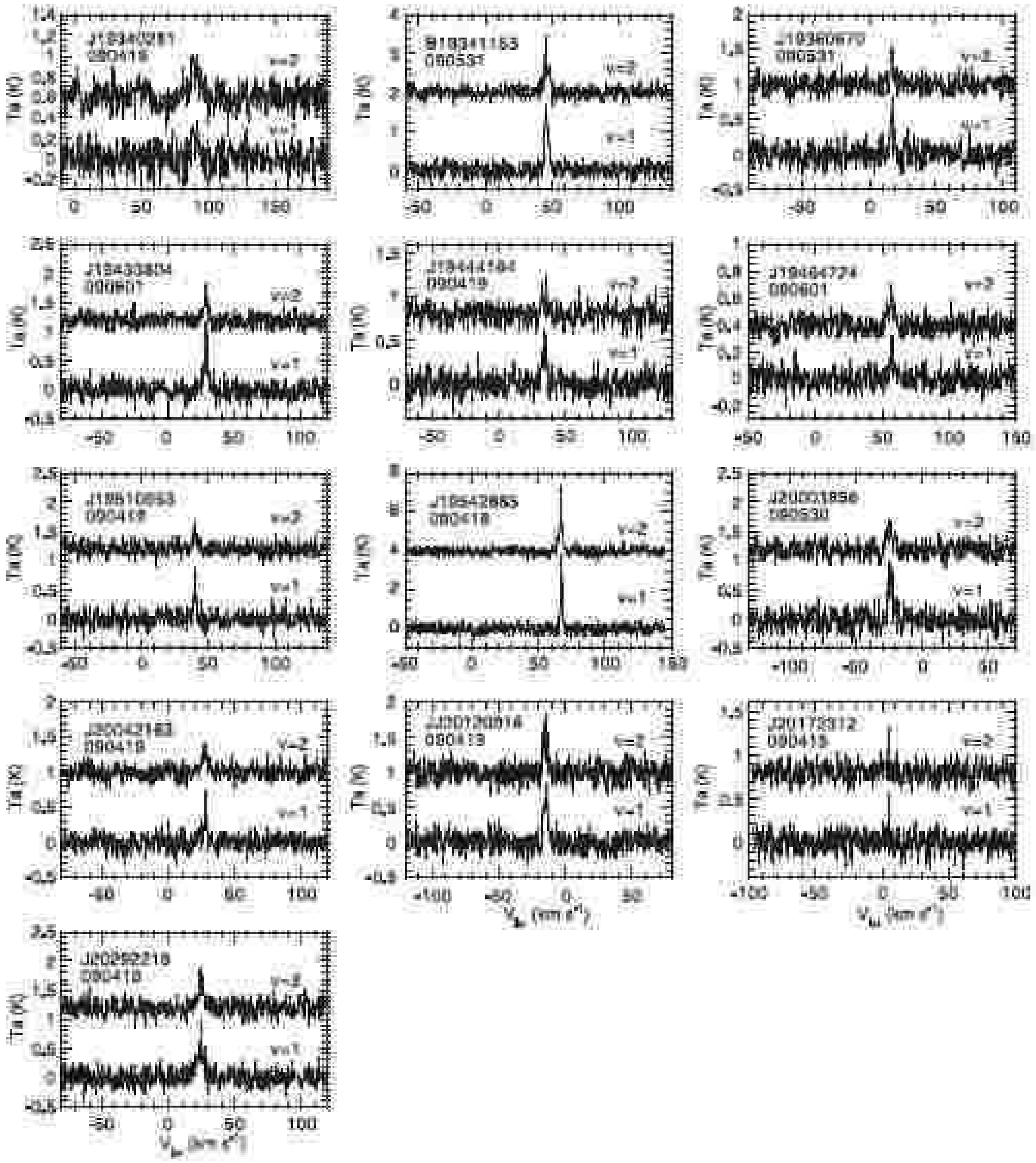

Fig. 1. e. SiO $J = 1$–0 $v = 1$ and 2 spectra. The source name (Jhhmmssss format) and the observed date (yymmdd format) are shown at the upper left of each panel.

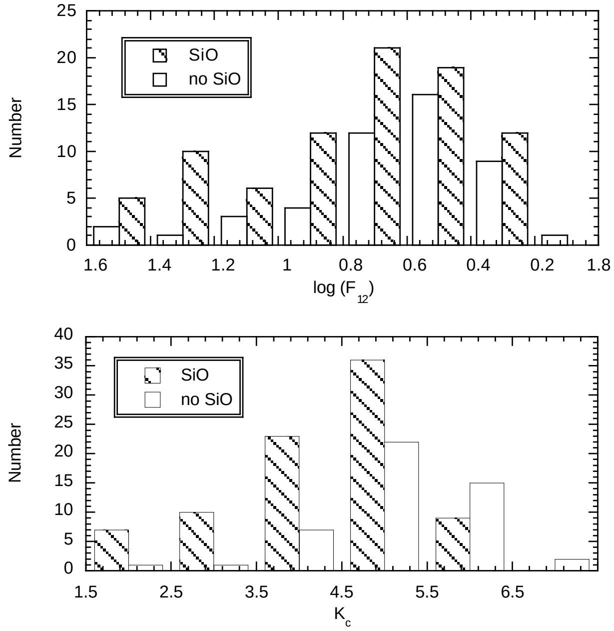

Fig. 3. histograms of $\log(F_{12})$ and K_c for SiO detections and no detections.

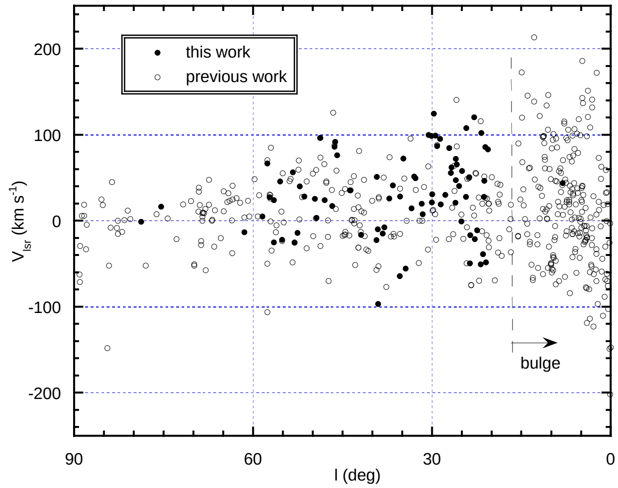

Fig. 4. Velocity-longitude diagram of SiO maser sources at $|b| > 3°$. Filled and unfilled circles indicate the SiO sources detected in this and the previous works, respectively. The vertical dashed line at $l = 17°$ indicates a gap of the velocity spread (see text).

3. Discussion

3.1. *Selection of the candidates in streaming*

Figure 4 shows a longitude-velocity diagram for the SiO sources found in this work (filled circles) and those in our past SiO surveys (unfilled circles). We can see a considerable increase of SiO detections in this sky region. A large vertical (velocity) spread of sources below $l = 17°$ in figure 4 is attributed to the Bulge stars. At $l \sim 17°$, there is a gap in the spread of radial velocities. Beyond $l = 18°$, the velocity spread increases again. The lack of stars beyond $V_{\rm LSR} \sim 50$ km s^{-1} at the gap indicates that it is the edge of the Galactic Bulge (at least, for the peanut-shape thick Bulge with $|b| > 3°$). Therefore, in this paper, we specially pay attention to the sources with $v_{\rm LSR} < 0$ in the region of $l = 18$–$40°$. Because the Galactic circular rotation gives positive $v_{\rm LSR}$ in the range $l = 0$–$90°$ (in the solar neighborhood), it is hard to separate any streaming motions, if present, at the $v_{\rm LSR} > 0$ side in this diagram. Note that the stars on the solar circle fall on the $v_{\rm LSR} = 0$ line in the l-v diagram (if they circularly rotate around the Galactic center with the circular velocity same as that of the Local Standard of Rest). Two concentrations of the $v_{\rm LSR} < 0$ stars are seen in figure 4: one around $l = 20$–$25°$, and another $l = 30$–$40°$. Beyond $l = 45°$, we also see a mild scatter of stars with large negative velocities. However, at the range beyond $l = 45°$, the stars in the distant spiral arms ($D > 11$ kpc at $l = 45°$) fall outside the solar circle and have the negative $v_{\rm LSR}$ in the l-v diagram. Therefore, it is more or less difficult to separate the streaming candidates beyond $l = 45°$ unless distances are accurately known.

For simplicity, we restrict the later discussion only to the stars with large negative velocities ($v_{\rm LSR} \lesssim -40$ km s^{-1}) in the longitude range between $l = 18$ and $40°$.

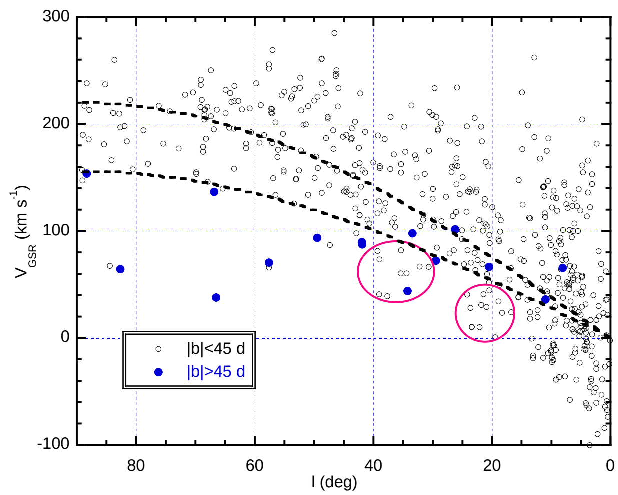

Fig. 5. Velocity-longitude diagram ($V_{\rm GSR} - l$). Filled and unfilled circles indicate the objects at high ($|b| > 45°$) and low ($|b| < 45°$) galactic latitudes. The broken curves indicates the $v_{\rm LSR} = 0$ line (figure 4) in the cases of $|b| = 0°$ (upper) and $45°$ (lower).

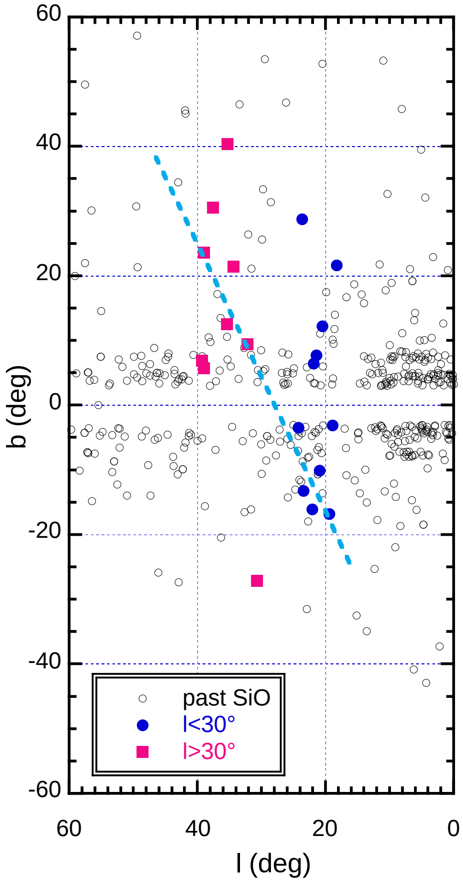

Fig. 6. Positions of the SiO sources in the Galactic coordinates. Filled and unfilled symbols indicate the deviant candidate and the usual disk star, respectively. The broken line indicates a possible orbital locus if they are interpreted as a debris stream (Deguchi et al. 2007).

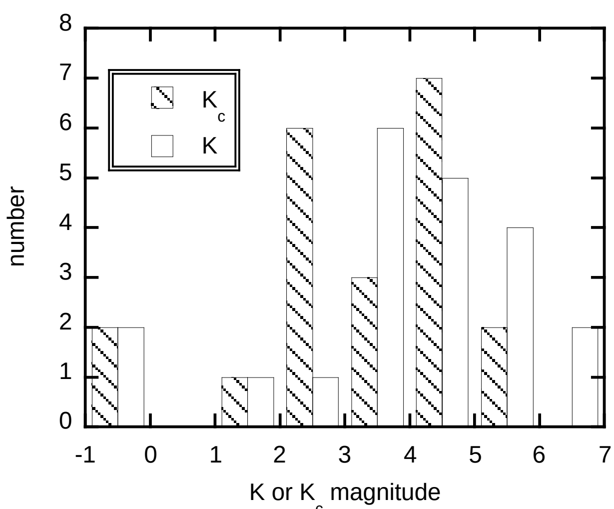

Fig. 7. Histogram of K_c (shaded) and K (unshaded).

However, it is not clear how to select the streaming candidates from usual stars with large random motion. To make the separation as definitive as possible, and to minimize the effects due to Galactic longitudes and latitudes, we made the plot (figure 5) by the velocity with respect to the Galactic Standard of Rest (GSR), where

$$v_{GSR} = v_{\rm LSR} + V_\phi \sin(l) \cos(b). \tag{2}$$

Here, we use the LSR rotational velocity around the Galactic center, $V_\phi = 220$ km s^{-1}. We apply, for the later use, the standard solar motion of 20 km s^{-1} in the direction of $R.A. = 18^h00^m00^s$ and $Dec. = 30°00'00''$ (1900.0) (*radio definition*) with respect to the Local Standard of Rest and the Sun – Galactic-center distance of 8.0 kpc. The two broken curves in figure 5 indicates the $v_{\rm LSR} = 0$ line in figure 4 in the cases of $|b| = 0$ (upper curve) and 45° (lower curve). For the current purpose of separating streaming candidates, we selected the stars under the lower broken curve between $l = 18$ and 40° excluding the objects with $|b| > 45°$; the candidates are in two ellipses. Figure 6 shows the sky positions of the candidates (filled circle) and else (open circles) in the Galactic coordinates. Because a boundary between the stars in random motion and the stars in streaming is not clear at present, we have chosen all the likely candidates, which are in the ellipses in figure 5, and investigate the nature of this subsample. In fact, we will see in the next section that all of these objects are highly likely objects in a stream.

The distribution of these candidate stars in the sky is shown in figure 6. It spreads widely in latitude ($\sim 60°$), but not much in longitude ($\sim 20°$). Infrared properties of these candidate stars are summarized in table 4. We created the magnitude-color and color-color diagrams of the candidates in near and middle-infrared bands (similar to figure 2), and compared the distribution with that of noncandidates. The candidates and noncandidates seem to have no clear difference in distribution in these diagrams, suggesting that the physical properties of the streaming candidates are not very different from those of normal disk SiO sources.

3.2. Kinematic property of the candidate stars and model fittings

Figure 7 shows histograms of apparent and corrected K magnitudes (K and K_c) for the candidates. The histogram of K_c shows triple peaks, indicating that the candidates can be separated into three groups according to their magnitudes: the bright group with $K_c = -1 - 0$, the middle group with $K_c = 1 - 4$, and the faint group with $K_c > 4$. Grouping into three may not be very meaningful due to statistical errors. However, let us separate the sample into three for convenience, and see if any useful properties reveal.

Figure 8 shows a comparison of observed radial velocities with the model velocities. It shows a clear trend that $V_{\rm GSR}$ for the observed stars decreases with K_c. The model velocity curve should have this tendency. Broken curves in each panel indicate the velocity variation with distance at $l = 20$, 30 and 40° for three different veloc-

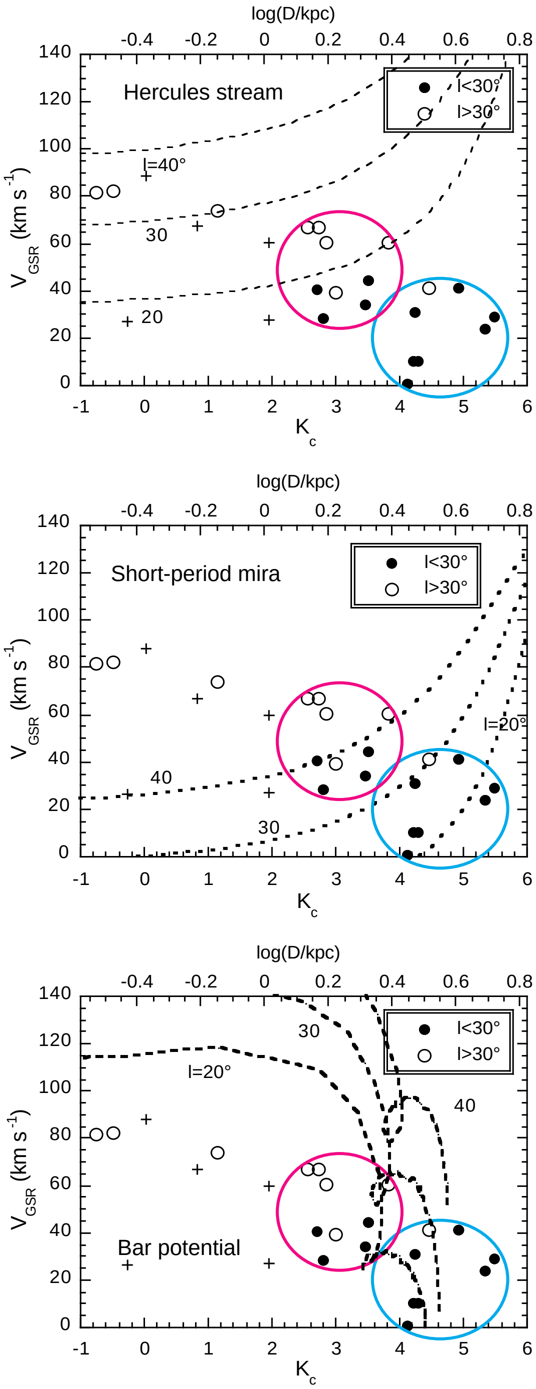

Fig. 8. Comparison of the velocity fittings for the diagram of $v_{\rm GSR}$ against K_c, where corrected magnitude, K_c, can be converted to a distance, as shown in the upper axis. Open and filled circles indicate the candidate SiO sources above and below $l = 30°$, and crosses indicate short-period miras at $20 < l < 70°$ [listed as Group 2 in Table 2 of Feast & Whitelock (2000). Three broken curves in the upper panel show plots of GSR velocities at $l = 20$, 30 and 40° (from lower to upper) for the Hercules stream stars with the most likely velocity of (V_R, V_ϕ)=(32 km s^{-1},185 km s^{-1}) at any radii. The broken curves in the middle panel show plots of GSR velocities at $l = 20$, 30 and 40° (from lower to upper) in the model with the velocity field (V_R, V_ϕ)=(75 km s^{-1}, 122 km s^{-1}) for short-period mira. The broken curves in the last panel show the case by the velocity field calculated using a damping bar potential (see in the text).

ity fields: the Hercules-stream (top panel), a short-period blue miras (middle), and a weak-bar model (last).

Here, the Hercules stream has a spatial velocity vector $(U, V, W)_{\rm LSR}$=(−31.8, −35.3, −0.8) in unit of km s^{-1} in the Local Standard of Rest frame (Famaey et al. 2005), where the U, V, and W axes are taken toward the Galactic center, toward the direction of Galactic rotation, and toward the Galactic north pole, respectively. Note that the spatial motion of the Hercules stream is known only in the solar neighborhood, and the extension of this stream is not known. Therefore we assumed for simplicity that the spatial velocities, V_R and V_ϕ (rotational and outward motions), are kept at any radii in the Galactic disk. The brightest 3 stars ($K_c < 2$) in the top panel fall in the area between two broken curves of $l = 30°$ and 40°. Therefore, these stars can be associated with Hercules moving group. However, the other fainter stars with $K_c > 2$ cannot belong to the same stream, if the given velocity field of the Hercules stream is extended to large distances. The Hipparcos catalog gives parallax and proper motion data for 3 stars in table 4; two of them are in a brightest star group. Calculated (U, V, W) velocity components for these two stars are compatible with the Hercules stream velocity components, though one star has negative parallax so that we assumed the distance of 300pc from the corrected K magnitude.

Middle panel of figure 8 shows a model fitting with a velocity field with $V_R = 75$ and $V_\phi = 122$ km s^{-1}, which have been proposed by Feast & Whitelock 2000 for short-period blue miras in the solar neighborhood. This velocity field seems to fit the stars with $K_c > 2$ and $l < 30°$, though it is not enough for the brightest stars with $K_c < 3$. Feast & Whitelock (2000) explained the large deviation of motion of short-period miras from the Galactic rotation by oval orbits with large eccentricity produced near the outer Lindblad resonance (OLR), and suggested that their sample is a mixture of the stars with variety of orbital parameters.

Last panel of figure 8 shows a fit by the velocity field influenced by a Bulge bar. The velocity fields are calculated on the basis of a weak-bar linear theory. A simple logarithmic gravitational potential with a few percent deformation due to bulge bar is utilized in the calculation; see equation (3-77) in Binney & Tremaine (1987). The theory gives a stellar orbit as a sum of two motions in a rotating frame: an epicyclic motion, and an oscillating motion produced by a periodic force due to a Bulge bar. The latter is regarded as a velocity field in the Galaxy uniquely determined only by the bar gravitational potential, but the former is determined by the initial conditions of stars and therefore includes arbitrarily randomness. We calculated the velocity field produced by the bar (the latter), and plotted this in the last panel of figure 8. In order to avoid too large deviations from the equilibrium position due to the Lindblad and corotation resonances, we introduced a damping constant of the bar potential for convenience, and make the velocity field calculable at any radii in the Galaxy (see Appendix 3 in detail). The parameters used in our model is summarized in Table 5 [see details of the

parameters in the more elaborate calculations of Habing et al (2006)].

The last panel of Figure 8 indicates that the most distant, most deviant stars (objects in the lower-right part of the panel), can be fit by the parameter ranges within a standard bar model. A schematic diagram (shown in figure 9) well explains why such a large deviation from the Galactic rotation occurs. The periodic orbit produced by the Bulge bar (in a rotational coordinate) is indicated by the thick ellipse between outer Lindblad and corotation radii. The star is located at the perigalacticon (small filled circle on the ellipse) when the major axis of the bar passes the guiding center of the rotating frame. Beyond the corotation radius, the bar pattern speed (~ 60 km s^{-1} kpc^{-1}) is faster than the circular rotational speeds of the stars in a standard model of the Galaxy bar; the periodic orbit is always retrograde. The star moves to the fourth quadrant of the ellipse (indicated by unfilled circle of figure 9) if the star concerned is located within 45 degree after the bar passage. Taking the effect of prograde rotation of the frame into account, the motion on the rest frame (in GSR) results the star motion toward the Sun. The magnitude of the velocity toward the Sun depends on the location of the stars in the Galaxy; the separation of the star from the bar major axis and the separation from the corotation and OLR.

The weak bar theory provides a reasonable explanation for the large negative velocities of the distant stars with $K_c = 3$–5. However, we found that the parameter values of the standard model does not give any good fits for brighter stars, which are located outside of the OLR. On the periodic orbit (thin ellipse in figure 11), the star comes at apogalacticon at the bar major-axis passage, and moves to the second quadrant in the ellipse. The rotational correction to the rest frame gives the star motion receding from the Sun. Because this is an opposite sense to the observation, we cannot get any good fit to the velocities of bright stars and Hercules group of stars by this model. Dehnen (2000) successfully explained the motion of Hercules group of stars with the bar model, though he assumed a slightly larger radius of the OLR (7.2 kpc). The OLR radius, which is close to the solar circular radius, makes line-of-sight changes of objects at the solar neighborhood dramatically, and the shear can produce a bimodal velocity distribution function as made in his model. In our calculation, we have neglected the effect of epicyclic motion which acts as a random motion, and introduced a suppression of resonances by decaying bar potential. The smaller radius of OLR and the damping assumption makes the computation simpler, but may lose a strictness of calculations near the OLR. In addition, the stellar orbits with large eccentricities are not involved in the linearized theory. In summary, the velocity field calculated on a basis of the weak-bar theory can give a good physical insight, and explain the observed stellar velocities for the distant stars reasonably well, though it is not for the nearby stars. Furthermore, it is possible that the sampling of nearest stars in the present sample is considerably biased due to small number.

3.3. *Motion perpendicular to the Galactic plane*

Our data shows that the deviant group of 20 selected stars spreads in latitude up to $|b| \sim 30^\circ$, and the average height ($\langle |z| \rangle$) is 0.5 kpc. These stars may be considered as members of the thick disk, which belong to older generations than members of thin disk. Binney (1981) considered the resonant excitation of star motion perpendicular to the Galactic plane due to periodic perturbation by the bar gravitational potential. This theory seems to explain well the observed spread of deviant candidate stars in latitude, at least qualitatively.

A basic equation describing the motion perpendicular to the Galactic plane is written as [equation (9) of Binney (1981)]

$$\ddot{z} + z\{\nu_0^2 + 2q'_A cos(\kappa t + \phi_0) + 2q'_B cos[2t(\Omega - \Omega_0)]\} = 0, \quad (3)$$

where q'_A and q'_B are constants determined by the orbital parameters of the epicyclic and forced motion on the Galactic plane, respectively. Here, ν_0 is a basic frequency of oscillation in z-direction, which is determined by the gravitational potential, and Ω and Ω_0 are the angular speed (a circular rotation) at the guiding center, and the bar pattern speed. Let us parametrize the constant ν_0 as

$$\nu_0 = u\Omega. \quad (4)$$

Here the parameter u describe the flatness of gravitational potential ($0 < u < 1$). Because the value of u is not well known for the case of our Galaxy, we assume $u = 0.5$. The value does not influence strongly on the later discussion.

The resonance excitation occurs when

$$\nu_0 = n\kappa/2, \quad \text{or} \quad (5)$$

$$\nu_0 = n(\Omega - \Omega_0), \quad (6)$$

where n is an integer. Using equation (4), above conditions can be rewritten for the Galaxy model with a flat-rotation-curve as

$$u = n/\sqrt{2}, \qquad or \quad (7)$$

$$\Omega = \Omega_0/[1 + u/(2n)]. \quad (8)$$

Because the first condition is satisfied only for a special potential parameter, we can neglect the z resonance on the epicyclic motion in our Galaxy. Because $\Omega < \Omega_0$ beyond the corotation radius, the second condition can be satisfied at various n near the corotation radius, for example, at radii 1.25 , 1.13, etc. times corotation radius. These resonant radii are approximately 4–5 kpc in our Galaxy.

The star develops large oscillations perpendicular to the equatorial plane in a time scale of 10 rotational periods due to resonant coupling (Binney 1981). Therefore, the observed displacement of maser sources from the Galactic plane seem to be consistent with the resonant coupling theory.

3.4. *Further considerations*

Though it is less likely, we investigated a possibility that these deviant stars are a part of a tidal stream of a disrupting dwarf galaxy. If it is a relic stream, these stars

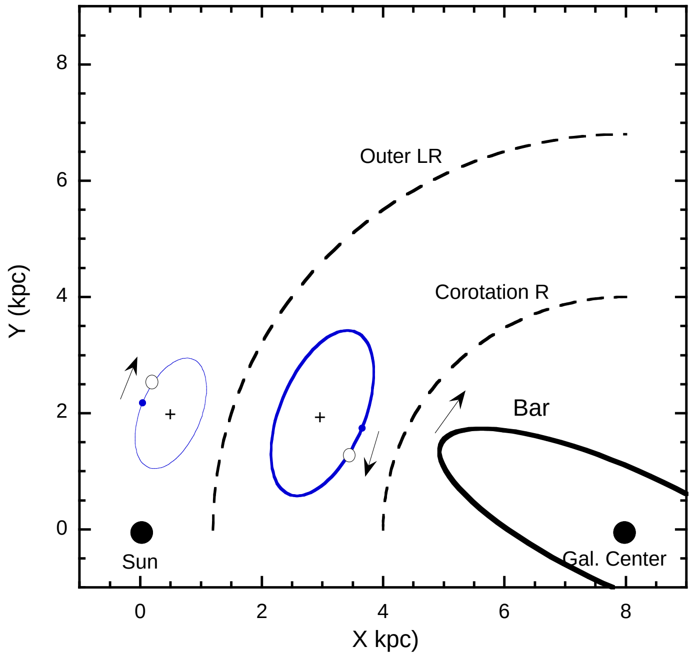

Fig. 9. Schematic diagram of the first quadrant of the Galaxy. The Sun is taken as the origin of the X and Y coordinates (indicated by large filled circle), and the X and Y axes toward the Galactic center and the direction of $l = 90°$. The thick line shows the Galactic Bar. Locations of the outer Lindblad and corotation resonances are indicated by broken lines. The ellipses shown in thin line indicate the stellar orbit seen in the rotating frame. The star comes on the minor axis (shown by small filled circle) when the bar major axis points toward the center of ellipse (indicated by cross), and it moves at the position shown by unfilled circle. Note that, when the guiding center crosses the resonance, the starting position changes their phase by 180° on the ellipse, and the direction of rotation changes.

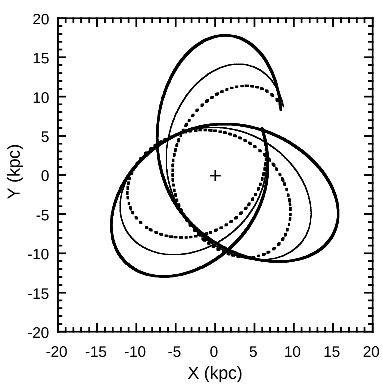

Fig. 10. Stellar orbits in a logarithmic potential (a face-on view to the orbital plane) in a rest frame. Thick, thin, dotted lines indicate stellar orbits with different angular momenta. The cross mark shows the center of the model galaxy. Unlike $1/r$ potential, the orbit has a smaller curvature inside, but a strong deflection at outer part.

must be aligned on a single locus orbiting our Galaxy. We have tried to fit the star positions and their radial velocities with a single orbit by a model gravitational potential with a flat rotation curve (without influence of a Bulge bar). However, we could not obtain any reasonable fits which satisfy both positions and radial velocities within allowable uncertainties in distance. The main reason is that the observational tendency of decreasing radial velocity with distance between ~ 0.3–6 kpc (as shown in figure 8) is hard to realize with any orbits in the assumed gravitational potential [$\sim log(r)$]. Unlike the $1/r$ potential, the orbital locus becomes more or less straight for stars near the corotation radius (see Figure 10) when the orbit is eccentric in the potential with a flat rotation curve. To have very small $v_{\rm GSR}$ near corotation radius (~ 4 kpc) as observed, the star must move in the direction perpendicular to the line of sight. To make a continuos locus of orbit from outer side to inside, the orbit must have a large curvature at the inside, which cannot make in the assumed potential.

Moreover, the deviant stars have infrared properties similar to those of usual disk SiO maser stars. Therefore, we deduce that the age and mass distributions of the deviant group are not very different from those of usual disk maser stars. The ages of these maser stars, which are at the AGB phase of stellar evolution, are deduced to be roughly a few Giga yr (for an initial mass of 1.5–2 $M_{\odot}$; Feast 2009). The stars experience the periodic variation of gravitational potential by the Bulge bar typically 10 times after their birth (~ 2 Gyr). This time scale is enough for these stars to be deviant from the Galactic rotation. Possibly, a short-period blue miras are more aged than average maser/infrared stars, so that the periodic oscillation of the Bulge bar potential appears to affect their motions more severely.

Though we have not completely consume all the possible orbits of tidal streams, we think that the deviant group of stars at various distances must comprise of different or-

bits, which may be a result of periodic perturbation by the Bulge bar. Therefore, all of these considerations support that the origin of the deviant motions of maser sources is a periodic perturbation of gravitational potential due to the Bulge bar.

4. Conclusion

We detected 84 out of 134 infrared objects off the Galactic plane by the SiO $J=1$–0 $v=1$ or 2 lines. Some of these objects exhibit large negative radial velocities particularly at $l=20-40^{\circ}$, where the Galactic rotation should give positive ones. Their distribution is scattered in the latitude range $\Delta b \sim 60^{\circ}$. This negative velocity group of stars spreads between 0.3 kpc to 6 kpc in distance. It is possible to interpret that the brightest part of this deviant group is the Hercules stream of stars found in the solar neighborhood, and slightly distant part of this group as a part of outward flow found in short-period mira, both of which have been explained by the resonance effect of the Bulge bar. Though our simple calculation of the velocity field based on weak bar theory cannot fit the velocities of the nearest group of selected stars, it successfully explains the large negative-velocity stars located between the outer Lindblad and corotation resonances. We have also shown that the resonant coupling due to the periodic perturbation of the Bulge bar can create the star motion perpendicular to the Galactic plane near the corotation resonance. These facts strongly suggest that the deviant group of stars is produced by the gravitational perturbation of the Bulge bar.

We thank Dr. Tsuyoshi Sakamoto for reading the manuscripts and useful comments. This research made use of the SIMBAD and VizieR databases operated at CDS, Strasbourg, France, and as well as use of data products from Two Micron All Sky Survey, which is a joint project of the University of Massachusetts and Infrared Processing and Analysis Center/California Institute of Technology, funded by the National Aeronautics and Space Administration and National Science foundation.

Appendix. 1. Individually interesting objects

- J12370691-1731319 (=T Crv): This is an M6 mira with a period 389d (Williams et al. 2004) at high Galactic latitude ($b=45^{\circ}$). A previous water maser search gives a negative result (Lewis 1997). We detected a strong SiO $J=1$-0 $v=1$ line but with no noticeable $v=2$ emission. The very low $v=2/v=1$ intensity ratio and blue IRAS color ($C_{12}=-0.37$) of this star fit well with the correlation of this ratio with the IRAS color which was found by Nakashima & Deguchi (2007). Volk et al. (1991) classified the IRAS LRS spectrum of this object as featureless ("F").
- J12583891+2308215 (=T Com): A previous SiO maser search for this object was negative (Nyman et al. 1986). OH masers have been detected by Nguyen-Q-Rieu et al. (1979) at $v_{\rm LSR}=9$ and 23 km s^{-1}. A later observation (Chengalur et al. 1993) found the 1612 MHz emission at $v_{\rm LSR}=23.2$ and 34.1 km s^{-1}, giving the average stellar velocity 28.7 km s^{-1}, which is consistent with the SiO radial velocity at 27.8 km s^{-1} in this paper. H_2O masers have been detected by Kleinmann et al. (1978) at 25.3 and 27.6 km s^{-1},
- J15591138+1939570 (=V336 Ser): This star exhibits featureless IRAS LRS spectrum (LRS class 13), and Guglielmo et al. (1997) classified this object as an M-type star. The detection of SiO masers of this star secures the oxygen richness of this star.
- J18205487+5031432 (=EO Dra = IRAS 18196+5030): This is an M7 star at high declination. The IRAS LSR spectrum of this star shows a strong 10 μm silicate emission giving an LRS class of 26. Sharples et al. (1995) made spectroscopic observation of this star deriving the radial velocity of $v_{\rm Helio} \sim -17$ km s^{-1} from the TiO band profile, which agrees well with the SiO maser velocity $v_{\rm LSR}=-1$ km s^{-1} in this paper. No reference of the previous radio observation was found for this star.
- J18213513+8238388 (IRAS 18276+8236): This is a relatively bright infrared source located closely to the celestial north pole. This objects exhibits strong 10 μm silicate emission (LSR class 29; Olnon et al. 1986). Cohen & Kuhi (1977) identified this IR object (AFGL 2171) to an M7III star. Radio searches for molecular lines had been negative (Zuckerman et al. 1978; Dinger et al. 1979; Nyman et al. 1992). We detected SiO masers at $v_{\rm LSR}=-27$ km s^{-1} for the first time.
- J19233466+0037583 (V850 Aql =IRAS 19210+0032): This s a D-type symbiotic star (Phillips 2007) with Hα emission (Allen & Glass 1974). This star was originally misclassified as a planetary nebula, but was corrected later (Sabbadin 1986; Acker et al. 1987). Searches for radio continuum emission at 5 and 14 GHz were made with negative results (Aaquist & Kwok 1990). No OH or H_2O maser search was made. We detected SiO masers in this star for the first time.
- J19340281+0926061 (IRAS 19316+0919): Engels & Lewis (1996) detected H_2O masers at $V_{\rm LSR}=78.5$ km s^{-1}. OH 1612 MHz maser was a single peak detection at $v_{\rm LSR}=76.4$ km s^{-1}, and OH main lines were not detected (Lewis 1997). We detected SiO masers at $V_{\rm LSR}=92$ km s^{-1}, establishing an accurate stellar velocity for this object.

Appendix. 2. Water maser observations

We also observed a few objects by the 22.235 GHz H_2O maser lines with the Nobeyama 45m telescope during the same period of SiO observations as a backup for bad weather condition. Though the H_2O maser observations are limited, interesting objects are involved. The HEMT

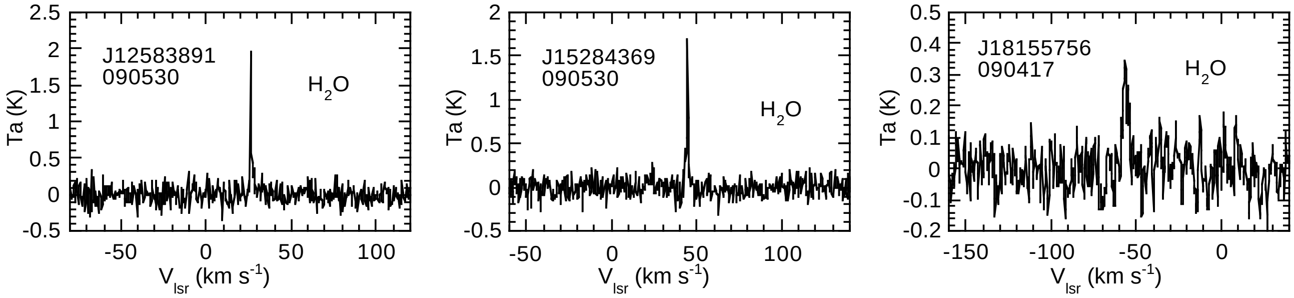

Fig. 11. H_2O maser spectra for the detected sources.

22GHz receivers was used for observations and the conversion factor of antenna temperature to flux density is about 3.0 Jy/K. We have detected 3 objects. The line parameters of the H_2O masers are given in table 6, and the line profiles are given in figure 11.

References

Aaquist, O. B. & Kwok, S. 1990, A&ASup. Ser., 84..229A

Acker, A., Chopinet, M., Pottasch, S. R., & Stenholm, B. 1987, A&ASup. Ser. 71, 163

Allen, D. A. & Glass, I. S. 1974, MNRAS, 167, 337

Binney, J. 1981, MNRAS, 196, 455

Binney, J., & Tremaine, S. 1987, Galactic Dynamics (Princeton Univ. Press, Princeton), p194

Belokurov. V. et al. 2007, ApJ, 657, L89

Bensby, T., Oey, M. S., Feltzing, S., & Gustafsson, B. 2007, ApJ, 655, L89

Bournaud, F., Combes, F., & Semelin, B. 2005, MNRAS, 364, L18

Chengalur, J. N., Lewis, B. M., Eder, J., & Terzian, Y. 1993, ApJS, 89, 189

Cohen, M. & Kuhi, L. V. 1977, PASP, 89, 829

Cutri, R.M., et al. 2003, 2MASS All Sky Catalog of Point Sources[1]

Deguchi, S., Fujii, T., Izumiura, H., Kameya, O., Nakada, Y., & Nakashima, J. 2000b, ApJS, 130, 351

Deguchi, S., Imai, H., Fujii, T., Glass, I., Ita, Y. et al. 2004, PASJ, 56, 261

Deguchi, S., Fujii, T., Ita, Y., Imai, H., Izumiura, H., et al. 2007, PASJ, 59, 559

Deguchi, S. 2008, proceeding of IAU sympo. No. 242 "Astrophysical Masers and their Environments", p200 ed. by J.M. Chapman & W.A. Baan, Cambridge Univ. Press

Dehnen, W. 2000, AJ, 119. 800

Dinger, A. S. C. Dickinson, D. F. Gottlieb, C. A. & Gottlieb, E. W. 1979, PASP, 91, 830

Egan M.P., Price S.D., Kraemer K.E., Mizuno D.R., Carey S.J., et al. 2003, Air Force Research Laboratory Technical Report AFRL-VS-TR-2003-1589

Eggen, O. J. 1996, AJ, 112, 1595

Engels, D. & Lewis, B. M. 1996, A&AS, 116, 117

Famaey, B., Jorissen, A., Luri, X., Mayor, M., Udry, S., Dejonghe, H., & Turon, C. 2005, A&A, 430, 165

Feast, M. W. 2009, Proceeding of the conference "AGB stars and Related Phenomena" held Nov. 2008, p48, Ed. by Ueta, T., Matsunaga, N., and Ita, T.

Feast, M. W.& Whitelock, P. A. 2000, MNRAS, 317, 460

Fujii, T., Deguchi, S., Ita, Y., Izumiura, H., Kameya, O., Miyazaki, A., & Nakada, Y. 2006, PASJ, 58, 529

Glass I. S., Whitelock P. A., Catchpole R. M., & Feast M. W. 1995, MNRAS, 273, 383

Grillmair, C. J. 2009, ApJ, 693, 1118

Guglielmo, F., Epchtein, N., Arditti, F., & Sevre, F. 1997, A&AS, 122, 489

Habing, H. J., Sevenster, M. N., Messineo, M., van de Ven, & G. Kuijken, K. 2006, A&A, 458, 151

Helmi, A., White, S. D. M., de Zeeuw, P. T., & Zhao, H. 1998, Nature, 402, 53

Helmi, A. et al. 2006, MNRAS, 365, 130

Hozumi, S. & Hernquist, L. 2005, PASJ, 57, 719

Ideta, M. & Hozumi, S. 2000, ApJ, 535, L91

Izumiura, H., Deguchi, S., Hashimoto, O., Nakada, Y., Onaka, T., Ono, T., Ukita, N., & Yamamura, I. 1995, ApJ, 453, 837

"IRAS Catalog of Point Sources, Version 2.0" NASA RP-1190, 1988

Kleinmann, S. G. Sargent, D. G., & Dickinson, D. F.1978, AJ, 83, 1206

Lewis, B. M. 1997, AJ, 114, 1602

Messineo, M., Habing, H. J., Menten, K. M., Omont, A. & Sjouwerman, L. O. 2004, A&A, 418, 103

Nakashima, J. & Deguchi, S. 2007, ApJ, 669, 446

Navarro et al. 2004, ApJ, 601, L43

Nguyen-Q-Rieu, Laury-Micoulaut, C., Winnberg, A., & Schultz, G. V. 1979, A&A, 75, 351

Nyman, L.-Å., Johansson, L. E. B., & Booth, R. S.1986, A&A, 160, 352

Nyman, L.-Å., Booth, R. S., Carlström, U., Habing,, H. J. Heske, A., Sahai, R., Stark, R., van der Veen, W. E. C. J., & Winnberg, A.1992, A&A. Sup. Ser., 93, 121

Olnon, F. M., & IRAS Science team, 1986, A&AS, 65, 607

Phillips, J. P. 2007, MNRAS, 376, 1120

Sabbadin, F. 1986, A&AS, 65, 301

Sevenster M.N., van Langevelde, H. J., Moody, R. A., Chapman J.M., Habing H.J., & Killeen, N.E.B., 2001, A&AS, 366, 481

Sharples, R. M., Whitelock, P. A., & Feast, M. W. 1995, MNRAS,.272, 139

Volk, K., Kwok, S., Stencel, R. E., & Brugel, E. 1991, ApJS, 77, 607

Wainscoat, R. J., Cohen, M., Volk, K., Walker, H. J., & Schwartz, D. E. 1992, ApJS, 83, 111

Williams, P.R., Wozniak, S.J., Vestrand, W.T., & Gupta, V. 2004, AJ, 128, 2965

Zuckerman, B., Palmer, P., Gilra, D. P., Turner, B. E., & Morris, M. 1978, ApJ, 220, L53

[1] *http://irsa.ipac.caltech.edu/applications/Gator/*

Appendix. 3. Theory of star motion in a weak bar potential

In a frame rotating with angular speed Ω, two-dimensional equations of motion for a test particle moving in the Galactic plane are written as

$$\ddot{x} = 2\Omega\dot{y} - \partial\Phi/\partial x + \Omega^2 x \tag{9}$$
$$\ddot{y} = -2\Omega\dot{x} - \partial\Phi/\partial y + \Omega^2 y \tag{10}$$

where Φ is a gravitational potential (see Binney & Tremaine 1987) and the origin of the coordinates is taken at the center of the Galaxy. For a weak bar-like potential with m-fold symmetry, the gravitational potential can be written as

$$\Phi = \Phi_0(r) + \Phi_1(r)\cos\{m[\theta - (\Omega_0 - \Omega)t]\} \tag{11}$$

where Ω_0 is the pattern speed of a bar, and θ is the angle of the particle position vector from the x-axis in the rotating frame. In this paper, we only consider a case of a weak bar potential, where the effect due the second term is small compared with the first term, i.e., $|\Phi_1(r)| \ll |\Phi_0(r)|$, and $m = 2$. The angular rotation speed of the frame is determined by the balance of centrifugal force with the 0th-order gravitational attraction,

$$\Omega^2 r_0 = (\partial\Phi_0/\partial r)|_{x=r_0, y=0} \tag{12}$$

Putting small deviations of the particle position from the equilibrium position ($x_0 = r_0$, $y_0 = 0$)

$$x_1 = x - x_0 \tag{13}$$
$$y_1 = y - y_0, \tag{14}$$

we obtain

$$\ddot{x}_1 = 2\Omega\dot{y}_1 + x_1[\Omega^2 - \partial^2\Phi_0/\partial r^2|_{x=r_0}] - \partial\Phi_1/\partial r|_{x=r_0}\cos(m\Omega_1 t) \tag{15}$$
$$\ddot{y}_1 = -2\Omega\dot{x}_1 - \Phi_1|_{x=r_0} m\sin(m\Omega_1 t)/r_0 \tag{16}$$

in the first order approximation, where $\Omega_1 \equiv \Omega_0 - \Omega$. For the case of a galaxy with a flat rotation curve, the gravitational potential can be written as

$$\Phi_0(r) = (v_0^2/2)\ln(a^2 + x^2 + y^2) \tag{17}$$

where v_0 is a circular rotation velocity of a particle (constant) and a is a core radius. The bar potential is often approximated (e.g., Habing et al 2006) as

$$\Phi = (v_0^2/2)\ln[a^2 + x^2(1-\epsilon) + y^2(1+\epsilon)]. \tag{18}$$

We set the bar potential $\Phi_1(r)$ as close as to the first order term in ϵ of the above equation,

$$\Phi_1(r) = -\epsilon v_0^2 r^2/(a^2 + r^2). \tag{19}$$

In such an approximation, we finally have equations of motion as

$$\ddot{x}_1 = 2\Omega\dot{y}_1 + (4\Omega^2 - \kappa^2)x_1 + B_x\cos(m\Omega_1 t) \tag{20}$$
$$\ddot{y}_1 = -2\Omega\dot{x}_1 + B_y\sin(m\Omega_1 t), \tag{21}$$

where

$$B_x = -\partial\Phi_1/\partial r|_{x=r_0} = 2\epsilon v_0^2 r_0\, a^2/(a^2 + r_0^2)^2 \tag{22}$$
$$B_y = -m\Phi_1|_{x=r_0}/r_0 = m\epsilon v_0^2 r_0/(a^2 + r_0^2), \tag{23}$$

and

$$\kappa^2 \equiv 3\Omega^2 + \partial^2\Phi_0/\partial r^2|_{x=r_0} = 2\Omega^2 \tag{24}$$

In the case of decaying bar potential, we use

$$\epsilon = \epsilon_0 \exp(-\gamma t), \tag{25}$$

where ϵ_0 is a constant. Note that the equations of motion (20) and (21) are linear with respect to x_1 and y_1 with additional forced oscillating terms. These equations have a general solution of linear combination of epicyclic and forced-oscillation terms,

$$x_1 = A_x\cos(\kappa t + \phi) + E_x(t)\exp(-\gamma t) \tag{26}$$
$$y_1 = A_y\sin(\kappa t + \phi) + E_y(t)\exp(-\gamma t), \tag{27}$$

where the epicyclic terms must satisfy the following condition

$$A_y = 2(\Omega/\kappa)A_x, \tag{28}$$

and A_x (or A_y) and ϕ are arbitrary constants determined by the initial condition, and the forced oscillation terms are expressed as

$$E_x(t) = [(N_{xcx}B_x + N_{xcy}B_y)\cos(m\Omega_1 t) + [(N_{xsx}B_x + N_{xsy}B_y)\sin(m\Omega_1 t)]/d_{xy} \tag{29}$$

$$E_y(t) = [(N_{ycx}B_x + N_{ycy}B_y)\cos(m\Omega_1 t) + [(N_{ysx}B_x + N_{ysy}B_y)\sin(m\Omega_1 t)]/d_{xy}. \tag{30}$$

Here, the denominator is calculated as

$$d_{xy} = [(m\Omega_1 - \kappa)^2 + \gamma^2][(m\Omega_1 + \kappa)^2 + \gamma^2](m^2\Omega_1^2 + \gamma^2)^2, \tag{31}$$

and the terms in numerators are written as

$$N_{xcx} = -(m^2\Omega_1^2 + \gamma^2)^2(m^2\Omega_1^2 - \kappa^2 - \gamma^2), \tag{32}$$

$$N_{xcy} = 2m\Omega\Omega_1(m^2\Omega_1^2 + \gamma^2)(m^2\Omega_1^2 - \kappa^2 - 3\gamma^2), \tag{33}$$

$$N_{xsx} = -2\gamma m\Omega_1(m^2\Omega_1^2 + \gamma^2)^2, \tag{34}$$

$$N_{xsy} = 2\gamma\Omega(m^2\Omega_1^2 + \gamma^2)(3m^2\Omega_1^2 - \kappa^2 - \gamma^2), \tag{35}$$

$$N_{ycx} = -2\gamma\Omega(m^2\Omega_1^2 + \gamma^2)(3m^2\Omega_1^2 - \kappa^2 - \gamma^2) \tag{36}$$

$$\begin{aligned} N_{ycy} &= 2\gamma m\Omega_1(m^4\Omega_1^4 + 8m^2\Omega^2\Omega_1^2 - 2\kappa^2 m^2\Omega_1^2 \\ &+2\gamma^2 m^2\Omega_1^2 - 4\kappa^2\Omega^2 - 8\gamma^2\Omega^2 + \kappa^4 + 2\gamma^2\kappa^2 + \gamma^4), \end{aligned} \tag{37}$$

$$N_{ysx} = 2m\Omega\Omega_1(m^2\Omega_1^2 + \gamma^2)(m^2\Omega_1^2 - \kappa^2 - 3\gamma^2), \tag{38}$$

$$\begin{aligned} N_{ysy} &= -m^6\Omega_1^6 + (2\kappa^2 - \gamma^2 - 4\Omega^2)\ m^4\Omega_1^4 \\ &+[(4\kappa^2 + 24\gamma^2)\Omega^2 - \kappa^4 - 4\gamma^2\kappa^2 + \gamma^4]\ m^2\Omega_1^2 \\ &+(-4\gamma^2\kappa^2 - 4\gamma^4)\Omega^2 + \gamma^2\kappa^4 + 2\gamma^4\kappa^2 + \gamma^6. \end{aligned} \tag{39}$$

The denominator, d_{xy}, is always positive at the Lindblad- and corotation-resonance radii (i.e., $m^2\Omega_1^2 - \kappa^2 = 0$ and $\Omega_1 = 0$), when the damping term ($|\gamma| > 0$) is introduced. Therefore stellar orbits are calculable at any radii as far as the deviation from the equilibrium position is small. Note that the cross terms, N_{xsx}, N_{xsy}, N_{ycx}, and N_{ycy} are proportional to γ. When $|\gamma|$ is much smaller than $|\Omega_1|$, these terms are negligible and the major axis of the elliptic orbit is oriented perpendicularly to the radial direction (as shown in Figure 9). However, near the resonance, these terms influence to the orientation of the elliptic orbit such as the major axis of the orbit is slightly inclined toward the radial direction of the Galaxy. This effect produces larger observed radial velocities of stars near the resonant position. It is well known in the limit of $\gamma = 0$ that the amplitude terms in equations (29) and (30) change sign when the equilibrium position crosses the Lindblad-resonances. Therefore, the phase of the particle in the elliptic orbit due to forced oscillation varies by 180 degree at the resonance (see Figure 9). However, this sudden change is moderated in the damping model, causing a cycling shape of the curves near the outer Lindblad resonance as shown in the last panel of Figure 8.

It is believed that bars in the gas-rich spirals are short lived (e.g., Bournaud et al. 2005). Furthermore, the effect of a triaxial halo, or a central massive blackhole may also destroy the bar within a Hubble time scale (Ideta & Hozumi, 2005; Hozumi & Hernquist 2005). Therefore, the decaying (or growing) bar model presented in this paper well facilitates to investigate stellar orbits near resonances in the Galaxy.

Table 1. Observational results of SiO Masers.

2MASS name	SiO $J=1$–0 $v=1$ line Ta (K)	$V_{\rm lsr}$ (km s^{-1})	L.F. (K km s^{-1})	rms (K)	SiO $J=1$–0 $v=2$ line Ta (K)	$V_{\rm lsr}$ (km s^{-1})	L.F. (K km s^{-1})	rms (K)	obs. date (yymmdd.d)
$J12370691-1731319$	1.473	−33.5	3.113	0.051	...	...	...	0.041	090531
$J12583891+2308215$	2.078	27.8	5.549	0.055	1.264	27.8	4.323	0.046	090531
$J15284369+0349430$	6.648	44.2	11.289	0.082	4.822	44.2	12.526	0.071	090529
$J15591138+1939570$	1.017	14.6	2.618	0.078	0.707	14.7	2.191	0.067	090531
$J16122976+2453570$	1.651	−16.8	5.091	0.083	1.401	−15.6	3.902	0.066	090531
$J16292643-1920509$	1.259	−9.2	4.769	0.084	0.482	−7.0	2.384	0.073	090529
$J16510590+1020515$	4.213	19.4	17.956	0.103	2.992	19.4	10.998	0.094	090531
$J16524821+0524269$	2.096	−46.3	9.523	0.058	0.668	−52.4	3.231	0.050	090529
$J16534478+4857022$	3.951	16.8	11.554	0.129	2.703	16.6	8.947	0.104	090531
$J17210403+2655505$	3.114	25.8	14.033	0.178	0.892	25.8	0.814	0.161	090530
$J17312879+3229525$	1.278	−24.8	7.159	0.112	1.160	−24.8	3.926	0.998	090530
$J17331391+0820390$	0.467	8.1	1.243	0.132	0.655	8.0	1.167	0.109	090417
$J17364445+1051070$	1.781	−55.3	5.434	0.208	2.074	−55.4	5.241	0.175	090530
$J18000391+2335371$	1.310	3.3	3.068	0.123	0.727	3.8	0.955	0.105	090530
$J18024911-0632355$	0.217	−39.1	0.290	0.062	0.267	−38.6	0.506	0.049	090601
$J18080907-0649058$	1.097	−50.4	2.094	0.227	1.147	−50.4	2.294	0.186	090417
$J18102890-0237427$	0.678	65.3	1.819	0.080	0.494	66.0	2.652	0.080	090419
$J18105856+0753085$	...	...	...	0.103	0.561	−64.1	1.217	0.082	090530
$J18110144-0142340$	0.440	63.1	2.012	0.080	0.376	61.4	1.265	0.070	090531
$J18120477-0607247$	0.265	120.7	0.595	0.043	0.247	120.5	0.767	0.038	040529
$J18155756+0120106$	0.543	21.3	3.232	0.089	0.358	21.6	2.483	0.068	090417
$J18162782-0425247$	2.177	57.7	4.115	0.288	2.086	58.6	3.711	0.239	090417
$J18170265-0720564$	0.434	−10.8	1.432	0.073	0.338	−10.9	1.344	0.066	090418
$J18192465-0439593$	0.214	1.0	1.262	0.046	0.159	−1.9	0.995	0.047	090418
$J18193355+0354498$	0.166	49.4	0.377	0.055	0.207	49.8	0.544	0.050	090418
$J18203449-0342095$	0.805	21.4	1.192	0.089	0.674	21.2	2.025	0.085	090418
$J18205487+5031432$	2.184	−0.7	5.533	0.160	1.365	−1.0	3.410	0.146	090531
$J18212420+0229022$	0.309	18.3	1.262	0.065	0.371	21.6	1.647	0.065	090418
$J18213513+8238388$	1.168	−27.0	3.210	0.123	0.583	−26.6	1.756	0.104	090531
$J18213854-0355447$	0.581	71.5	3.090	0.080	0.593	72.8	2.598	0.069	090529
$J18223249-0305115$	0.470	55.9	1.111	0.078	0.381	55.7	0.589	0.069	090418
$J18231986+0929569$	0.597	−14.4	1.514	0.058	0.613	−15.3	1.174	0.056	090418
$J18250570-0032320$	0.517	99.1	1.762	0.069	0.381	99.1	1.896	0.064	090418
$J18253335+0856472$	0.326	−7.6	0.900	0.052	0.200	−7.6	0.902	0.045	090529
$J18264298-0024486$	0.282	125.0	0.876	0.056	0.192	124.8	0.839	0.048	090531
$J18274403+0025128$	0.962	99.6	2.578	0.153	0.833	100.1	2.022	0.118	090417
$J18302847+0523383$	0.712	28.3	2.580	0.124	0.595	28.4	1.606	0.096	090417
$J18331997+0425410$	0.980	73.1	3.135	0.093	0.643	72.2	2.872	0.077	090531
$J18354242+0905384$	1.006	51.4	2.662	0.072	0.895	51.3	2.440	0.068	090418
$J18364611+0845469$	0.989	−9.7	2.518	0.105	0.630	−9.8	2.140	0.093	090531
$J18384242+0541298$	0.652	40.8	2.482	0.102	0.604	41.5	2.251	0.080	090531
$J18420916+0801180$	0.303	−96.4	0.564	0.057	0.410	−97.1	1.882	0.064	090418
$J18454767-1148074$	0.983	102.6	1.449	0.067	0.958	102.4	2.168	0.090	090418
$J18501116-1007570$	0.329	55.2	1.952	0.056	0.218	46.6	1.187	0.049	090601
$J18512520+1202084$	0.386	35.2	1.250	0.067	0.367	36.1	1.531	0.060	090418
$J18523817+1733113$	0.264	97.7	1.179	0.056	0.125	95.9	0.317	0.048	090531
$J18524262-0951445$	0.339	108.0	1.047	0.081	...	...	...	0.070	090601
$J18530987-1329244$	0.599	85.0	1.725	0.070	0.399	87.2	1.079	0.399	090417
$J18550366-1328438$	0.437	29.3	1.322	0.078	0.447	26.8	0.882	0.066	090601
$J18554765-1415207$	0.650	83.1	1.498	0.082	0.338	83.6	0.547	0.069	090601
$J18572211-0831208$	...	...	...	0.084	0.320	47.6	1.020	0.081	090418
$J18572648+1349096$	0.566	76.2	0.523	0.130	...	...	...	0.105	090417
$J18575917+1413196$	0.500	86.2	1.303	0.103	0.551	86.6	0.985	0.093	090418
$J18594368-0924127$	0.576	39.7	1.010	0.131	0.450	41.5	0.519	0.129	090418

Table 1. (Continued.)

2MASS name	SiO $J=1$–0 $v=1$ line Ta (K)	$V_{\rm lsr}$ (km s^{-1})	L.F. (K km s^{-1})	rms (K)	SiO $J=1$–0 $v=2$ line Ta (K)	$V_{\rm lsr}$ (km s^{-1})	L.F. (K km s^{-1})	rms (K)	obs. date (yymmdd.d)
$J19004752-0742491$	0.273	84.7	0.681	0.083	...	...	...	0.073	090419
$J19010471-1050004$	0.376	28.1	1.487	0.089	0.442	28.3	1.614	0.080	090419
$J19010944+1538566$	0.738	24.3	1.800	0.086	0.340	24.2	1.316	0.076	090530
$J19012574-0529398$	1.014	87.3	3.152	0.096	0.569	87.3	1.694	0.081	090419
$J19020569-1236483$	0.430	−21.4	1.058	0.068	0.432	−20.7	1.280	0.061	090530
$J19024407-0611124$	0.538	95.6	0.688	0.083	0.337	95.3	0.422	0.075	090419
$J19050061+2310298$	0.486	−23.1	2.548	0.084	0.732	−21.0	2.427	0.077	090419
$J19054911-1212243$	1.253	−16.8	3.917	0.123	0.979	−16.4	3.563	0.114	090419
$J19062439-1509534$	0.990	−48.7	2.833	0.114	1.088	−48.	2.997	0.099	090601
$J19074038-0515161$	0.415	99.0	0.574	0.063	...	...	...	0.056	090601
$J19085920-1510032$	1.315	46.7	2.900	0.107	0.761	46.7	1.289	0.761	090419
$J19090454+2939292$	3.692	−13.4	10.319	0.105	2.520	−12.8	5.419	0.091	090530
$J19094939-0804034$	0.333	30.0	0.991	0.059	0.251	30.8	0.678	0.056	090601
$J19111079-0227493$	0.481	51.2	1.379	0.066	0.213	52.1	0.675	0.055	090601
$J19211169+0320578$	0.283	−21.1	0.683	0.064	0.333	−23.3	0.785	0.064	090419
$J19233466+0037583$	1.674	26.1	4.442	0.128	1.143	26.3	1.085	0.115	090419
$J19234517+7141137$	3.018	13.7	8.656	0.189	5.438	14.3	15.792	0.169	090531
$J19240522-0722442$	0.589	31.2	1.061	0.116	0.495	31.3	1.030	0.100	090531
$J19340281+0926061$	0.367	92.2	0.974	0.097	0.431	91.9	2.237	0.090	090419
$J19341153+1958285$	1.616	45.5	5.349	0.124	1.480	46.0	4.511	0.101	090531
$J19360670+0945041$	0.811	17.5	1.919	0.112	0.586	17.3	1.512	0.093	090531
$J19433804+1403158$	1.177	28.3	2.897	0.151	0.630	28.5	1.648	0.098	090601
$J19444164+0513039$	0.618	34.8	1.674	0.096	0.441	36.4	1.012	0.090	090419
$J19464724+1549014$	0.322	56.7	0.752	0.064	0.331	56.9	0.852	0.058	090601
$J19510953+1354375$	0.932	40.7	1.566	0.099	0.468	39.7	1.079	0.087	090419
$J19542885+1943430$	3.802	66.7	7.192	0.162	3.300	66.7	7.487	0.138	090419
$J20003856+1331331$	0.975	−25.8	3.096	0.166	0.489	−25.0	1.638	0.122	090530
$J20042163+1748345$	0.734	28.1	1.746	0.091	0.445	27.3	1.734	0.080	090419
$J20120916+1116516$	0.867	−13.8	2.811	0.109	0.753	−13.9	2.735	0.096	090419
$J20172312+1718459$	0.614	5.2	1.101	0.093	0.566	5.0	1.228	0.092	090419
$J20292219+1311116$	0.973	24.1	3.790	0.107	0.102	24.2	2.699	0.071	090419

Table note: "Ta" is the antenna temperature at the intensity peak.
"$V_{\rm lsr}$" is the radial velocity in the Local Standard of Rest frame.
"L.F." is the integrated line intensity.
"rms" is the root mean square of the noise level.

Table 2. negative results.

2MASS name	SiO v=1 *rms* (K)	SiO v=2 *rms* (K)	obs. date (yymmdd.d)
$J16322460-1312013$	0.093	0.079	090531
$J16521876-1830343$	0.103	0.088	090531
$J17171484-0230186$	0.059	0.049	090529
$J17551370+1143462$	0.074	0.062	090529
$J18042450-0802252$	0.083	0.078	090419
$J18135847-0815296$	0.072	0.080	090418
$J18182494-0331378$	0.177	0.141	090531
$J18240372+0636258$	0.143	0.118	090417
$J18243205-0132065$	0.069	0.057	090529
$J18270226-0106095$	0.152	0.131	090530
$J18275079+0752206$	0.072	0.064	090418
$J18283699+0936501$	0.104	0.084	090531
$J18294430+0104534$	0.072	0.080	090418
$J18295773+0114056$	0.071	0.061	090530
$J18414435+0802164$	0.085	0.075	090531
$J18421582+0731314$	0.075	0.667	090418
$J18431907+0733137$	0.067	0.059	090418
$J18465164-1157048$	0.081	0.075	090418
$J18495300-1104202$	0.084	0.069	090601
$J18530734-1155310$	0.194	0.164	090417
$J18562524-0744227$	0.109	0.119	090418
$J18574985+2031371$	0.361	0.296	090417
$J19030151+1656312$	0.093	0.080	090531
$J19034074-1409330$	0.097	0.091	090419
$J19060940+1738007$	0.084	0.072	090531
$J19062416+1739313$	0.053	0.047	090530
$J19102783-1541355$	0.066	0.056	090601
$J19105141-0328410$	0.119	0.099	090419
$J19134664-0326081$	0.118	0.107	090419
$J19141725-0850549$	0.074	0.064	090419
$J19145484-0225287$	0.104	0.087	090530
$J19173939-1322488$	0.082	0.071	090531
$J19181178-0721437$	0.071	0.061	090601
$J19182271-0242108$	0.116	0.102	090419
$J19222258-1418050$	0.100	0.098	090419
$J19265373-0104251$	0.110	0.100	090419
$J19410829+0202312$	0.084	0.084	090531
$J19433664+1049180$	0.118	0.102	090531
$J19483842+2759358$	0.076	0.060	090530
$J19492572+0231306$	0.115	0.093	090530
$J19552508+0156036$	0.121	0.098	090601
$J19553800-0018428$	0.122	0.105	090530
$J19554049+1805361$	0.089	0.076	090419
$J19595639+1151450$	0.128	0.111	090531
$J20030250+0544166$	0.091	0.076	090419
$J20075461+1842544$	0.089	0.084	090419
$J20080544+1516428$	0.105	0.088	090531
$J20571628+0258445$	0.056	0.060	090601

Table note: "*rms*" is the root mean square of the noise level.

Table 3. Infrared properties of the observed sources.

2MASS name	l (°)	b (°)	K^*	$H-K$	K_c	IRAS	F_{12} (Jy)	C_{12}	v(SiO)$^\sharp$ (km s^{-1})
$J12370691-1731319$	298.083	45.211	2.598	0.765	2.216	12345−1715	34.50	−0.373	−33.5
$J12583891+2308215$	325.571	85.690	3.270	0.736	2.930	12562+2324	33.70	−0.233	27.8
$J15284369+0349430$	8.103	45.840	3.364	0.858	2.848	15262+0400	46.20	−0.175	44.2
$J15591138+1939570$	33.459	46.526	3.449	0.664	3.213	15569+1948	10.60	−0.433	14.6
$J16122976+2453570$	41.919	45.074	2.789	0.700	2.501	16103+2501	17.40	−0.321	−16.2
$J16292643-1920509$	357.592	19.667	2.381	0.689	2.109	16265−1914	28.90	−0.385	−8.1
$J16322460-1312013$	3.227	22.945	4.132	0.604	3.982	16296−1305	9.88	−0.216	
$J16510590+1020515$	28.565	31.385	3.023	0.652	2.804	16487+1025	10.50	−0.353	19.4
$J16521876-1830343$	1.790	15.928	3.698	0.740	3.352	16494−1825	3.28	−0.320	
$J16524821+0524269$	23.691	28.777	3.020	0.650	2.804	16503+0529	20.40	−0.276	−49.3
$J16534478+4857022$	75.428	39.124	2.938	0.774	2.543	16524+4901	16.80	−0.303	16.7
$J17171484-0230186$	19.371	19.590	5.786	0.772	5.394	17146−0227	2.36	−0.153	
$J17210403+2655505$	49.629	30.754	2.450	0.711	2.146	17190+2658	33.30	−0.310	25.8
$J17312879+3229525$	56.557	30.105	2.956	0.731	2.623	17296+3231	29.40	−0.361	−24.8
$J17331391+0820390$	31.591	21.153	7.726	2.078	5.454	17308+0822	12.00	0.021	8.1
$J17364445+1051070$	34.420	21.452	3.134	0.698	2.849	17343+1052	37.60	−0.360	−55.3
$J17551370+1143462$	37.298	17.715	6.345	0.818	5.887	17528+1144	4.80	−0.184	
$J18000391+2335371$	49.353	21.334	2.940	0.819	2.481	17579+2335	62.70	−0.243	3.5
$J18024911-0632355$	21.477	7.713	5.468	0.870	4.935	18001−0632	4.51	−0.157	−38.8
$J18042450-0802252$	20.343	6.649	5.465	0.786	5.053	18016−0802	5.94	−0.324	
$J18080907-0649058$	21.870	6.418	4.941	0.990	4.235	18054−0649	10.60	−0.118	−50.4
$J18102890-0237427$	25.870	7.881	7.663	2.156	5.278	18078−0238	7.52	−0.010	65.7
$J18105856+0753085$	35.444	12.556	4.220	0.776	3.823	18085+0752	21.70	−0.219	−64.1
$J18110144-0142340$	26.755	8.190	5.081	0.940	4.447	18084−0143	3.15	−0.331	62.2
$J18120477-0607247$	22.950	5.888	4.787	0.859	4.270	18094−0608	6.49	−0.112	120.6
$J18135847-0815296$	21.285	4.464	5.009	0.793	4.587	18112−0816	6.06	−0.149	
$J18155756+0120106$	30.061	8.501	4.436	0.771	4.046	18134+0119	13.80	−0.238	21.5
$J18162782-0425247$	24.974	5.723	5.960	1.499	4.521	18138−0426	20.40	0.013	58.2
$J18170265-0720564$	22.449	4.223	6.654	1.131	5.745	18143−0722	5.42	−0.158	−10.9
$J18182494-0331378$	25.999	5.710	5.745	0.954	5.091	18157−0332	4.91	−0.273	
$J18192465-0439593$	25.103	4.960	8.060	2.031	5.855	18167−0441	7.55	−0.066	−0.4
$J18193355+0354498$	32.797	8.872	8.763	2.303	6.167	18170+0353	5.58	−0.082	49.6
$J18203449-0342095$	26.095	5.152	4.489	0.835	4.007	18179−0343	5.15	−0.326	21.3
$J18205487+5031432$	78.759	25.285	3.224	0.723	2.903	18196+5030	27.00	−0.321	−0.9
$J18212420+0229022$	31.720	7.814	5.897	1.087	5.052	18188+0227	5.87	−0.273	20.0
$J18213513+8238388$	114.678	27.842	3.029	0.941	2.394	18276+8236	44.70	−0.175	−26.8
$J18213854-0355447$	26.018	4.811	5.643	0.913	5.048	18189−0357	4.53	−0.161	72.2
$J18223249-0305115$	26.871	5.003	6.132	1.503	4.688	18199−0306	9.43	−0.022	55.8
$J18231986+0929569$	38.293	10.523	4.584	0.838	4.097	18209+0928	9.88	−0.139	−14.9
$J18240372+0636258$	35.743	9.080	8.602	2.545	5.657	18216+0634	10.10	0.256	
$J18243205-0132065$	28.484	5.278	4.988	0.818	4.530	18219-0133	3.76	−0.350	
$J18250570-0032320$	29.434	5.610	4.766	0.755	4.399	18225−0034	7.22	−0.323	99.1
$J18253335+0856472$	38.034	9.787	6.166	0.859	5.649	18231+0855	4.80	−0.145	−7.6
$J18264298-0024486$	29.736	5.309	6.508	1.271	5.398	18241−0026	3.66	−0.142	124.9
$J18270226-0106095$	29.158	4.921	3.553	1.516	2.090	182444−0108	21.20	−0.453	
$J18274403+0025128$	30.597	5.465	6.672	1.654	5.010	18251+0023	14.40	−0.105	99.8
$J18275079+0752206$	37.313	8.803	6.734	1.380	5.467	18254+0750	6.22	0.064	
$J18283699+0936501$	38.980	9.404	6.089	0.820	5.628	18262+0934	4.50	−0.123	
$J18294430+0104534$	31.418	5.321	5.382	1.166	4.423	18271+0102	5.76	0.091	
$J18295773+0114056$	31.581	5.341	7.051	2.191	4.616	18274+0112	7.31	0.004	
$J18302847+0523383$	35.369	7.111	5.160	1.121	4.266	18280+0521	12.10	−0.182	28.3
$J18331997+0425410$	34.824	6.041	4.748	0.852	4.241	18308+0423	4.88	−0.329	72.6
$J18354242+0905384$	39.291	7.605	5.874	1.021	5.124	18333+0903	8.25	−0.041	51.3
$J18364611+0845469$	39.110	7.223	5.306	1.001	4.585	18343+0843	4.45	−0.217	−9.8

Table 3. (Continued.)

2MASS name	l (∘)	b (∘)	K^*	$H-K$	K_c	IRAS	F_{12} (Jy)	C_{12}	$v(\mathrm{SiO})^\sharp$ (km s^{-1})
$J18384242+0541298$	36.564	5.416	5.345	0.989	4.641	18362+0538	3.94	−0.032	41.2
$J18414435+0802164$	39.010	5.799	6.551	0.791	6.132	18393+0759	3.41	−0.215	
$J18420916+0801180$	39.042	5.700	4.923	0.812	4.474	18397+0758	8.27	−0.239	−96.8
$J18421582+0731314$	38.609	5.453	6.968	1.732	5.194	18398+0728	8.89	0.055	
$J18431907+0733137$	38.752	5.232	6.396	1.123	5.499	18408+0730	8.22	−0.248	
$J18454767-1148074$	21.774	−4.118	4.843	0.929	4.225	18429−1151	6.25	−0.024	102.5
$J18465164-1157048$	21.758	−4.418	8.119	1.928	6.063	18440−1200	5.47	−0.070	
$J18495300-1104202$	22.880	−4.683	6.355	0.886	5.799	18471−1107	3.09	−0.164	
$J18501116-1007570$	23.755	−4.326	5.492	0.818	5.034	18474−1011	3.07	0.015	50.9
$J18512520+1202084$	43.674	5.460	5.087	0.869	4.556	18490+1158	9.06	−0.024	35.7
$J18523817+1733113$	48.782	7.648	6.421	0.815	5.967	18504+1729	3.18	−0.267	96.8
$J18524262-0951445$	24.278	−4.759	4.914	0.753	4.550	18499−0955	5.76	−0.344	108.0
$J18530734-1155310$	22.472	−5.775	5.632	1.001	4.911	18503−1159	14.40	−0.246	
$J18530987-1329244$	21.068	−6.482	5.981	1.003	5.257	18503−1333	10.20	−0.199	86.1
$J18550366-1328438$	21.284	−6.890	5.543	0.925	4.931	18522−1332	4.94	−0.117	28.0
$J18554765-1415207$	20.661	−7.393	6.154	1.170	5.189	18529−1419	3.80	−0.006	83.3
$J18562524-0744227$	26.594	−4.622	5.425	1.350	4.201	18537−0748	7.80	−0.026	
$J18572211-0831208$	25.998	−5.184	6.518	1.321	5.336	18546−0835	6.15	−0.004	47.6
$J18572648+1349096$	45.936	4.950	8.039	2.776	4.762	18551+1345	57.80	−0.261	76.2
$J18574985+2031371$	52.022	7.854	5.634	1.203	4.622	18556+2027	14.60	−0.358	
$J18575917+1413196$	46.357	5.013	7.449	1.777	5.610	18556+1409	5.72	−0.090	86.4
$J18594368-0924127$	25.469	−6.099	5.539	0.841	5.048	18569−0928	7.19	−0.233	40.6
$J19004752-0742491$	27.106	−5.577	5.072	0.993	4.362	18580−0747	23.20	−0.140	84.7
$J19010471-1050004$	24.330	−7.034	7.288	1.943	5.210	18582−1054	13.70	−0.047	28.2
$J19010944+1538566$	47.982	4.972	5.092	0.786	4.680	18588+1534	8.74	−0.372	24.2
$J19012574-0529398$	29.167	−4.719	4.629	0.837	4.144	18587−0534	13.90	−0.214	87.3
$J19020569-1236483$	22.830	−8.045	4.918	0.810	4.472	18593−1241	6.48	−0.145	−21.0
$J19024407-0611124$	28.694	−5.321	5.444	0.761	5.068	19000−0615	6.18	−0.036	95.4
$J19030151+1656312$	49.343	5.155	6.797	0.949	6.150	19007+1652	4.30	−0.072	
$J19034074-1409330$	21.596	−9.068	6.465	1.130	5.558	19008−1414	6.15	−0.162	
$J19050061+2310298$	55.161	7.529	4.800	0.778	4.400	19029+2305	6.41	−0.167	−22.0
$J19054911-1212243$	23.604	−8.682	6.395	1.407	5.089	19030−1217	9.94	−0.132	−16.6
$J19060940+1738007$	50.302	4.801	7.520	2.093	5.226	19039+1733	3.92	−0.165	
$J19062416+1739313$	50.351	4.760	5.891	0.858	5.375	19041+1734	6.30	−0.185	
$J19062439-1509534$	20.967	−10.099	6.576	1.254	5.490	19035−1514	3.82	−0.031	−48.3
$J19074038-0515161$	30.087	−5.998	6.476	1.242	5.408	19050−0520	3.14	−0.045	99.0
$J19085920-1510032$	21.237	−10.662	5.867	1.054	5.069	19061−1514	8.31	−0.108	46.7
$J19090454+2939292$	61.454	9.565	2.130	0.622	1.954	19071+2934	26.10	−0.207	−13.1
$J19094939-0804034$	27.795	−7.736	5.058	0.908	4.470	19071−0808	6.79	−0.132	30.4
$J19102783-1541355$	20.909	−11.209	5.746	0.777	5.347	19075−1546	3.79	−0.348	
$J19105141-0328410$	32.041	−5.903	6.061	0.905	5.478	19082−0333	5.54	−0.309	
$J19111079-0227493$	32.986	−5.514	6.493	1.251	5.412	19085−0232	3.46	−0.041	51.7
$J19134664-0326081$	32.411	−6.533	5.068	0.833	4.588	19111−0331	8.63	−0.131	
$J19141725-0850549$	27.583	−9.072	4.819	0.803	4.383	19115−0856	6.25	−0.296	
$J19145484-0225287$	33.447	−6.328	8.125	1.988	5.982	19122−0230	9.29	0.304	
$J19173939-1322488$	23.802	−11.792	4.712	0.821	4.250	19148−1328	9.22	−0.201	
$J19181178-0721437$	29.367	−9.279	6.395	0.831	5.918	19155−0727	3.14	−0.225	
$J19182271-0242108$	33.593	−7.225	7.020	1.185	6.034	19157−0247	8.88	−0.093	
$J19211169+0320578$	39.326	−5.071	6.519	1.626	4.898	19186+0315	15.50	0.088	−22.2
$J19222258-1418050$	23.449	−13.221	5.598	1.400	4.302	19195−1423	8.78	0.170	
$J19233466+0037583$	37.181	−6.855	5.395	0.778	4.995	19210+0032	5.96	−0.350	26.2
$J19234517+7141137$	103.152	23.178	2.836	0.989	2.132	19243+7135	48.50	−0.349	14.0
$J19240522-0722442$	30.010	−10.595	4.897	0.776	4.500	19213−0728	8.75	−0.253	31.2
$J19265373-0104251$	36.036	−8.376	5.682	1.000	4.962	19243−0110	9.73	−0.166	

Table 3. (Continued.)

2MASS name	l (∘)	b (∘)	K^*	$H-K$	K_c	IRAS	F_{12} (Jy)	C_{12}	v(SiO)$^\sharp$ (km s^{-1})
$J19340281+0926061$	46.225	−5.022	6.822	1.347	5.602	19316+0919	6.06	−0.263	92.1
$J19341153+1958285$	55.483	0.036	4.004	0.771	3.614	19320+1951	27.40	−0.265	45.8
$J19360670+0945041$	46.748	−5.317	5.789	0.877	5.246	19337+0938	3.34	−0.199	17.4
$J19410829+0202312$	40.505	−10.086	6.011	1.058	5.207	19386+0155	17.40	0.435	
$J19433664+1049180$	48.588	−6.412	7.929	1.570	6.388	19412+1042	3.89	−0.030	
$J19433804+1403158$	51.421	−4.830	5.367	0.788	4.952	19413+1356	3.89	−0.262	28.4
$J19444164+0513039$	43.769	−9.360	4.806	0.751	4.445	19422+0505	5.33	−0.386	35.6
$J19464724+1549014$	53.336	−4.618	7.676	1.549	6.165	19445+1541	3.76	−0.098	56.8
$J19483842+2759358$	64.082	1.141	3.685	0.607	3.531	19466+2751	27.80	−0.011	
$J19492572+0231306$	41.935	−11.683	7.208	0.790	6.790	19469+0223	4.79	−0.061	
$J19510953+1354375$	52.207	−6.486	5.909	0.758	5.537	19488+1346	5.38	−0.154	40.2
$J19542885+1943430$	57.650	−4.222	5.547	1.555	4.028	19522+1935	29.30	−0.055	66.7
$J19552508+0156036$	42.133	−13.280	5.741	1.338	4.534	19528+0148	51.50	−0.164	
$J19553800-0018428$	40.121	−14.390	5.971	0.768	5.585	19530-0026	5.18	−0.313	
$J19554049+1805361$	56.385	−5.302	6.059	1.312	4.890	19534+1757	5.29	0.101	
$J19595639+1151450$	51.510	−9.366	5.159	0.774	4.764	19575+1143	10.20	−0.241	
$J20003856+1331331$	53.048	−8.667	5.143	0.792	4.723	19583+1323	14.20	−0.192	−25.4
$J20030250+0544166$	46.496	−13.097	5.855	0.792	5.435	20005+0535	7.16	−0.112	
$J20042163+1748345$	57.217	−7.216	4.771	0.821	4.309	20020+1739	8.51	−0.215	27.7
$J20075461+1842544$	58.441	−7.456	7.471	1.493	6.041	20056+1834	17.50	0.012	
$J20080544+1516428$	55.511	−9.303	7.593	1.326	6.404	20057+1507	3.28	−0.194	
$J20120916+1116516$	52.564	−12.232	6.824	1.793	4.962	20097+1107	6.47	0.005	−13.9
$J20172312+1718459$	58.463	−10.109	5.710	0.907	5.124	20151+1709	8.03	−0.237	5.1
$J20292219+1311116$	56.526	−14.779	4.939	0.900	4.363	20270+1301	7.86	−0.270	24.2
$J20571628+0258445$	51.363	−26.113	8.405	1.727	6.638	20547+0247	45.50	−0.129	

* The 2MASS photometric uncertainties are about 0.2 mag for bright stars with $K < 4$; see, *http://www.ipac.caltech.edu/2mass/releases/allsky/doc/sec2_2.html* .

$^\sharp$ "v(SiO) is the average radial velocity of SiO maser lines.

Table 4. Candidates for the deviant motions ($|b| > 3°$).

2MASS name	IRAS name	l (∘)	b (∘)	$v_{\rm LSR}$ (km s^{-1})	K	$H-K$	K_c	F_{12} (Jy)	C_{12}
$J16254746+1853328^\dagger$	16235+1900	35.35	40.35	−15.0	−0.63	1.09	−0.49	499.8	−0.44
$J16524821+0524269^*$	16503+0529	23.69	28.78	−49.3	3.02	0.65	2.80	20.4	−0.28
$J17071761+1710228$	17050+1714	37.70	30.52	−76.6	3.06	0.54	3.00	7.6	−0.22
$J17081033-0220225$	17055−0216	18.30	21.63	−40.6	6.21	1.11	5.34	6.4	−0.08
$J17354000+1535122$	17334+1537	38.98	23.63	−53.0	1.69	0.88	1.14	154.0	−0.18
$J17364445+1051070^*$	17343+1052	34.42	21.45	−55.3	3.13	0.70	2.85	37.6	−0.36
$J17450262-0512365$	17423−0511	20.49	12.23	−30.6	3.62	0.58	3.50	8.8	−0.30
$J18024911-0632355^*$	18001−0632	21.48	7.71	−38.8	5.47	0.87	4.94	4.5	−0.18
$J18080907-0649058^*$	18054−0649	21.87	6.42	−50.4	4.94	0.99	4.24	10.6	−0.12
$J18105856+0753085^*$	18085+0752	35.44	12.56	−64.1	4.22	0.78	3.82	21.7	−0.22
$J18163694+0341352^\dagger$	18141+0340	32.26	9.43	−49.0	2.70	0.49	2.72	7.8	−0.43
$J18364919-1351561$	18339−1354	18.94	−3.11	−36.9	3.60	0.59	3.47	13.8	−0.37
$J18382111+0850030^\dagger$	18359+0847	39.35	6.90	−57.0	−0.82	0.46	−0.76	409.0	−0.45
$J18420916+0801180^*$	18397+0758	39.04	5.70	−96.8	4.92	0.81	4.47	8.3	−0.24
$J18475335-0919102$	18450−0922	24.23	−3.45	−49.4	4.03	1.41	2.71	80.3	−0.14
$J19062439-1509534^*$	19035−1514	20.97	−10.10	−48.3	6.58	1.25	5.49	3.8	−0.03
$J19222258-1418050^*$	19195−1423	23.45	−13.22	−74.6	5.60	1.40	4.30	8.8	0.17
$J19291840-1916199$	19263−1922	19.47	−16.78	−69.3	4.22	0.57	4.12	11.9	−0.19
$J19310440-1640135$	19281−1646	22.12	−16.11	−69.5	5.05	1.09	4.21	24.7	−0.11
$J20261323-1347584$	20234−1357	30.72	−27.14	−33.3	3.24	0.98	2.55	46.7	−0.02

* detection in this work.

† Hipparcos proper motion data exists.

Table 5. Parameters used for the bar model

parameter	value
rotational velocity of the LSR	220 km s^{-1}
Galactocentric distance of the Sun	8 kpc
pattern speed of the bar	55 km s^{-1} kpc^{-1}
angle between bar major axis and the Sun-GC line	30°
radius of the corotation	4 kpc
radius of the outer Lindblad resonance	6.8 kpc
strength of the bar ($\epsilon/2$)	0.025
bar damping constant	4.1 km s^{-1} kpc^{-1}

Table 6. Observational results of H_2O Masers.

2MASS name	T_a (K)	$V_{\rm lsr}$ (km s^{-1})	L.F. (K km s^{-1})	rms (K)	obs. date (yymmdd.d)
$J12370691-1731319$	...	...	...	0.066	090530
$J12583891+2308215$	1.967	26.5	3.077	0.117	090530
$J15284369+0349430$	1.683	44.7	1.472	0.102	090530
$J16521876-1830343$	...	...	...	0.094	090417
$J17331391+0820390$	...	...	...	0.095	090417
$J18080907-0649050$	0.345	−56.5	1.333	0.063	090417
$J18155756+0120106$	...	...	...	0.065	090417